The Influence of Initial Angular Momentum on the Orbital and Structural Evolution of Satellite Subhalos in a Milky Way-like Dark Matter Halo

Théo Chérel

Division of Astrophysics
Department of Physics

Lund University

2026-EXA266

Degree project of 60 higher education credits
June 2026

Supervisors: Santi Roca-Fàbrega & Corentin Cadiou

Division of Astrophysics
Department of Physics
Box 118
SE-221 00 Lund
Sweden

Abstract

This thesis investigates how modifying the initial angular momentum (AM) condition of a Milky Way-like dark matter halo affects the orbital and structural properties of its satellite subhalos. This work uses a suite of five dark-matter-only (DMO) cosmological zoom-in simulations, the `VINTERGATAN-GM-AM`, in which the initial AM of the Lagrangian patch is modified using the `genetIC` code to obtain the following set of initial conditions relative to the fiducial simulation; $AM_{fid} \times \{0.5, 1.05, 1.1, 1.2, 2.0\}$. The evolution is initialized at $z = 99$ and ends at $z = 0$, and we use `ROCKSTAR` to extract subhalo information for our analysis.
In order to proceed, we develop a method to identify, match and track three subhalo candidates around our central halo. Using this limited sample size, we provided an analysis of the evolution of four properties in subhalos - the specific orbital AM, the virial radius, the virial mass and the radial distance to the central halo.
In our results, it is found that the specific orbital AM is strongly sensitive to the modification of the main halo's initial AM and that this sensitivity is persistent throughout the entire redshift range studied($z \sim 6$ to $z = 0$), with the ordering being set by the initial conditions. Moreover, the structural properties of the subhalos - the virial radius and mass - are shown to be largely insensitive to initial condition variations. Indeed, the virial radius of each run is shown to deviate by less than 10% compared to the reference run $AM_{fid}\times$ $\{1.1\}$. At low redshift, more significant deviations are observed and these are attributed to tidal stripping, occurring during orbital inspirals - an analysis of the radial distances show notable differences between simulation runs and the effect of the initial conditions modifications on the trajectory.
The results of this work show that modifying the initial AM condition leaves a persistent effect on the orbital properties of the subhalos. However, it provides evidence for little direct effect on the virial radius and virial mass evolution. Overall, the results present a physically consistent and coherent picture of the interplay between different dynamical processes in a purely gravitational environment, and are consistent with the predictions of Tidal Torque Theory (TTT) and the existing literature.

Contents

Acknowledgements

I would like to first thank my supervisor Santi Roca-Fàbrega and my co-supervisor Corentin Cadiou for all their help throughout the thesis. I appreciate their insights, which were priceless, and their patience, which was limitless. I learned more than I could have hoped for from them about the topic as well as scientific writing.

I also thank all those in the Galaxy Formation and Evolution Group here at Lund University. They assisted me on my journey and were there to help me when needed. My peers were also there to help me and I would like to show immense gratitude for all they have done for me, creating a great work environment. A special thanks is passed onto Isak Lindh who helped me countless times to parcel through my code (YT) and troubleshoot alongside me.

Finally, I would like to thank my friends and family who were there with me at all times. For my parents, to whom I owe too much, words are simply not enough. My brother and sisters who helped keep my motivation high. My nephews who patiently listened to me while I tried to explain the topic of the thesis. My grandparents and extended family who have always supported me in my academic journey.

Thank you.

Summary

When we look at the night sky, not only do we see far into the cosmos - distant stars and galaxies - but also deep into the past. The reason for this is that light takes years to travel from the stars and galaxies to us. And in fact, not only are they far from us, but they continue to move further away from us. One may wonder, why are these stars so far from us and why do we even have objects such as stars and galaxies in what seems to be empty space - the answer lies at the beginning of time.

When the universe began, it looked nothing like what we have today. The matter in our universe that creates the flower out in the garden or the mountains in the Himalayas or the rocks on the moon, was originally spread out. One may think that all that we can see and touch is all the matter that exists in the universe, but there is actually a form of matter that is hidden to us which we have never been able to observe, but that we know exists because it is able to pull the matter that we can see through gravity. We are thus able to infer its existence. This matter also was spread out, but not perfectly, and in time, as the universe grew, these imperfections led to clumps of this invisible matter.

Studying dark matter in isolation is particularly powerful, as it only interacts through gravity. This means we are able to remove all the other ways in which regular matter interacts (electromagnetism, thermally, and so on). These clumps would later be homes to galaxies and mini-galaxies that orbit around them. These dark matter homes are called dark matter halos and our current understanding tells us that they are rotating. The goal of this project was to investigate how the rotation of the dark matter halo of a Milky Way sized galaxy would affect the movement and internal properties of the dark matter halos of the mini-galaxies orbiting around it. We call the dark matter halos of the mini-galaxies, subhalos. This is interesting to us because as our telescopes become more powerful, we are able to see these mini-galaxies better. These satellite galaxies have a lot of dark matter compared to regular matter, which makes them important probes for better understanding dark matter, which we know very little about. It is therefore important to understand how the properties of these subhalos are affected by the different physics involved - including changing the rotation of the central halo.

In our project, we did our investigation using computer simulations. There were five computer simulations of the universe with a zoom-in on a single Milky Way sized galaxy that were run with slightly different initial rotations. We developed an algorithm to select three subhalos and compared how their properties changed and evolved in each of the simulation runs.

What we found was that changing the initial rotation of the central halo had a long lasting impact on the orbit of the subhalo. A stronger rotation of the central halo means a larger orbital angular momentum throughout the evolution of the subhalo. We also found that the internal properties such as its size and mass are largely unaffected by this initial change. Most of the difference we observe can be explained by the

differences in the trajectories of the subhalo orbits. When the subhalo gets close to the central halo, the latter pulls at the subhalos and rips parts of them away.
In this way, we were able to get a better understanding of how the properties of subhalos change when one changes the rotation of the central halo. As we look to the future, more powerful telescopes and specific space missions will provide us with better observations of these satellite galaxies, which will contribute to uncovering the mystery around dark matter.

Chapter 1

Introductions

Angular momentum is a fundamental property of dark matter halos, and understanding how it shapes the properties of satellite subhalos is essential for building a complete picture of dark matter halo evolution. Indeed, while its existence has been inferred through gravitational effects, the fundamental nature of dark matter remains poorly understood. Satellite subhalos - smaller dark matter halos orbiting within a host halo - are particularly interesting as they host dwarf galaxies whose low baryonic mass fractions make them especially sensitive probes of the dark matter distribution. Understanding how these structures form and evolve may therefore help better constrain dark matter properties. Moreover, as our observational capabilities improve and we begin to observe satellite populations around Milky Way-like galaxies, understanding what drives their properties becomes increasingly important. Specifically, this work examines how modifying the initial angular momentum of a Milky Way-like dark matter halo impacts the evolution of the orbital and structural properties of its satellite subhalos.

This analysis was done using data from `VINTERGATAN-GM-AM`, a suite of five DMO cosmological zoom-in simulations in which only the AM of the central halo is modified between runs. We select three subhalos to study and track them in all five simulation runs (see Sect. 2.4), and examine their properties to see how they evolve.

In this chapter we establish the scientific and historical context in galaxy formation and evolution theory necessary to introduce our central research topic. We begin by discussing the history of the field, including the comparison projects that have been undertaken in the past in order to motivate the genetically modified simulation approach adopted in our work. We then present the theoretical framework underlying our project such as the λCDM cosmological model, dark matter halo formation and the role of angular momentum in galactic dynamics. Finally, we state the specific research goals, providing the essential background needed to interpret the results presented in later chapters.

1.1 History and Context

The 1940s saw one of the first examples of galaxy simulation by Swedish astronomer Erik Holmberg, which relied entirely on light bulbs and photocells (Holmberg, 1941). He noticed that gravitational forces scaled in the same manner as the light intensity as a function of distance.

$$I \propto F_g \propto \frac{1}{r^2}$$

He thus produced an N-body model, where 2 galaxies were represented by 36 light bulbs. Each bulb had photocells recording the received light intensity from which he could determine the forces, and therefore induced dynamics on the bulb. By sequentially moving the bulbs and taking snapshots, he was able to produce one of the first galaxy merger simulations. The observations from his experiments, such as those regarding tidal features, were later confirmed to be accurate (Toomre & Toomre (1972); Biviano (2000)).

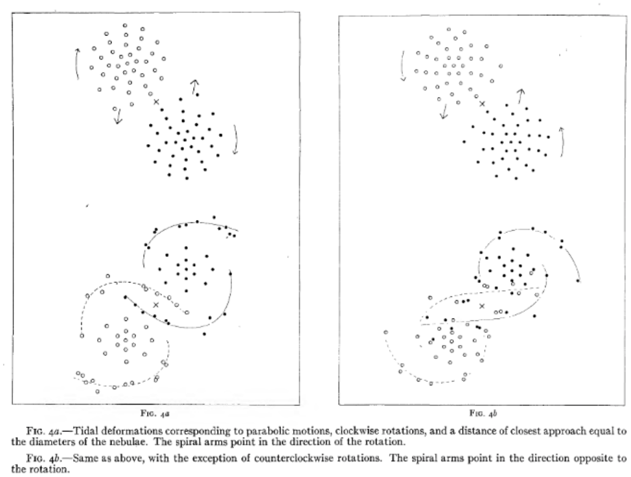

Figure 1.1: Schema taken from Holmberg, E. in Astrophysical Journal presenting the Galaxy Merger results from his experiments

This experiment led to the emergence of a growing sub-field in astrophysics; galaxy formation and evolution theory. This field seeks to understand the different physical mechanisms and processes that drive the assembly of galaxies and their morphologies. As with many topics in astrophysics, galaxy formation and evolution finds its roots in observational findings. It then became increasingly more active with computers which allowed for digitally rendered simulations and more particles to be used.

The growing role of computation in astrophysics is best illustrated by the rapid development of numerical simulations. The first astrophysical simulations were created in the 1960s (von Hoerner, 1960) and soon followed those answering questions of galaxy formation. In 1999, the Santa Barbara Cluster Comparison Project (Frenk et al., 1999) was proposed to address the issues of reproducibility in astrophysics. By comparing galaxy cluster models with the same initial conditions for a large variety of codes, it revealed the importance of juxtaposing different hydrodynamic simulations of the same astrophysical systems.

Similar projects from around the world, tackling this fundamental roadblock in the field of astrophysical simulations have been launched since such as the AQUILA and AGORA projects. These comparison projects provide a good forum for improving the quality of the results found by the different simulation codes by removing biases and leaving more room for understanding how the code framework might affect the results.

Our work follows a similar philosophy, comparing simulations in controlled environments: rather than comparing different codes, we compare different genetically modified initial conditions within the same code framework (RAMSES). Specifically, we compare the different scenarios of the VINTERGATAN-GM-AM suite of simulations.

1.2 Theory

1.2.1 λCDM Model

The current prevailing theory of cosmology is the λCDM model. This is due to its successes in describing the formation and evolution of the large scale structures of our universe, comparing with observational findings (such as with the Planck satellite observations of the Cosmic Microwave Background(CMB) Aghanim et al. (2020)) and characterizing the matter distribution of the universe(see Fig. 1.2).

The model has two foundational elements which describe it. The λ in the name refers to the model's inclusion of dark energy - a currently unobserved form of energy driving the expansion of the universe. The other half of the model relates to its description of the dark matter(DM) nature. Dark matter refers to the matter in the universe that does not interact electromagnetically and therefore is not observable directly by means of ground or space based instruments that rely on electromagnetism. On the other hand, DM does interact gravitationally and its presence has been inferred due to cosmological phenomena that cannot be described when considering purely baryonic matter - matter made up of protons and neutrons - which therefore does not interact with photons. Indeed, DM describes the unexpected (if one considers a baryonic matter distribution of galaxies) observed dynamics of galaxies which show that the rotational velocities of galaxies remain relatively constant at large distances from the galactic center. Among other discrepancies that DM manages to resolve (gravitational lensing differences in observation and theory, CMB anisotropies,...), this is strong evidence for the presence of DM in our universe. In the name, "CDM" refers to the Cold Dark Matter (CDM). As opposed to Warm Dark Matter (WDM) and the Hot Dark Matter (HDM) descriptions of dark matter. The key differences between these three descriptions of DM reside in the time these particles spend being relativisitc. Indeed, HDM outlines particles that stay relativistic far beyond the early universe, remaining so into the formation of galaxy-size masses. WDM is described to become non-relativisitic earlier. One major flaw with these theories of DM is that they fail to explain and characterize the smaller scale structures of the universe, such as dwarf galaxies. The small scale fluctuations would be smoothed out by the free streaming DM particles that would still be moving at significant velocities around the time of galaxy-size structure formation (Blumenthal et al., 1984). CDM differs in that it becomes non-relativistic very early on and therefore limits the effect of free streaming in smoothing out the small scale structures of the universe. It is therefore a prevalent theory, which successfully explains a wide range of cosmological and astrophysical observations.

At the foundation of this theory is a characterization of DM. Today our understanding of DM is still quite limited and direct detection of it is not possible, however indirect methods have given us an indication to how it is arranged in our universe.

1.2.2 Overview of Dark Matter Halos and Galaxy Formation

Observations of the current day inferred DM structures indicate that they are distributed in halos. Within these halos are subhalos that are smaller and gravitationally bound to them. A picture of a simulated DM

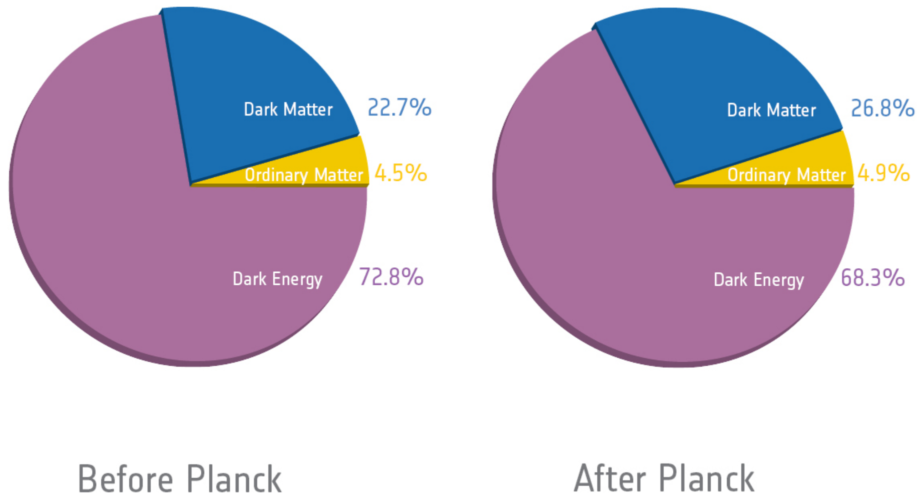

Figure 1.2: Pie chart based on Planck mission results showing the relative contributions of baryonic matter, dark matter, and dark energy Planck Collaboration & ESA (2013a)

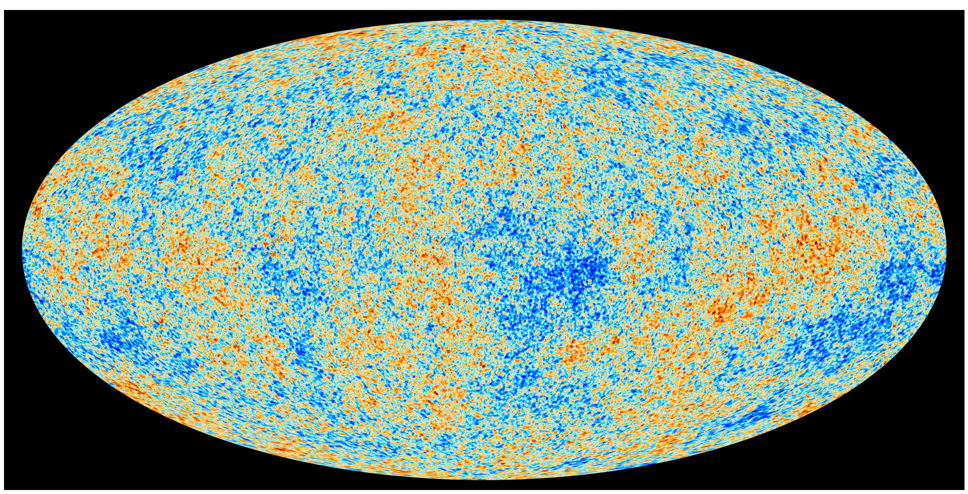

Figure 1.3: Image of the CMB and its anisotropies pictured by the Planck Mission Planck Collaboration & ESA (2013b)

halo with satellites orbiting around it is given in Fig. 1.4. The λCDM model describes this halo substructure by presenting a bottom-up hierarchical picture of halo structure formation. The following theoretical background on dark matter halos and structure formation follows closely Mo et al. (2010b). The classical picture of DM halo and galaxy formation is presented in the following steps:

1. Initially, after the early universe small DM perturbations expand with the universe

2. These small scale perturbations grow until they reach an over-density threshold and collapse under the process described spherical collapse theory (sect.1.2.3)

3. The DM halo virializes and enters an equilibrium state

4. The DM halo acquires angular momentum via tidal torques from surrounding matter

5. Gas accretes onto the halo and the gas shocks heat the halo which leads to radiative cooling

6. At the center of the halo, an angular momentum supported disc forms due to the spin up caused by angular momentum conservation and radiative cooling

7. At high enough pressures, stars form and the galaxy is defined

This picture of galaxy formation explains how the initial density perturbations in the early universe lead to the formation of galaxies. Indeed, these perturbations grow with the expansion on the universe and can be described using linear theory to form the large scale structures of the universe. These perturbations can be defined as an over-density field $\delta(\mathbf{x}, t)$ with the following formula:

$$\delta(\mathbf{x}, t) = \frac{\rho(\mathbf{x}, t) - \rho_0(t)}{\rho_0(t)}$$

where $\rho(\mathbf{x})$ is the local matter density and $\rho_0(t)$ is the mean background density of the universe at time t. These initial perturbations are directly observable today in the form of the CMB (see Fig. 1.3). They provide observational constraints which are used in cosmological simulations such as those used in this work. The growth of the perturbations can be described using the following formula for the over-density field:

$$\delta(\mathbf{x}, t) = \delta_0(\mathbf{x}) D(t)$$

where $\delta_0(\mathbf{x})$ is the over-density field linearly extrapolated to the present time and $D(t)$ is the normalized linear growth rate. Once these over-densities reach critical threshold $\delta_c = 1.686$, they collapse under their own self-gravity into virialized DM halos through self-gravity as described by the spherical collapse model which is discussed in more depth in sect.1.2.3.

It is important to make the distinction linear and non-linear regimes in the description of the formation of the physical structures. Indeed, while the early growth of perturbations is described by linear theory, their subsequent evolution enters the non-linear regime which requires different solutions. When entering the non-linear regime, the cycloid solutions described by the spherical collapse model in sect.1.2.3 become relevant. While the spherical collapse model is one simplified model, other more in depth models exist such as homogeneous ellipsoid models. Moreover, numerical techniques have allowed us to go beyond these limited analytical models and give more accurate solutions to the linear growth equation.

Above we have a picture of how DM haloes form hierarchically in the canonical ΛCDM picture. This opposes other models that have been proposed in the past. Indeed, such a model was suggested by Gunn (1977), which described galactic discs forming before the formation of their DM haloes. Over the years, this perspective of galaxy formation has been superseded due to its limitations in accommodating certain physical phenomena, such as differences in timescales of baryonic and DM collapse in the early universe (White & Rees, 1978). Fall & Efstathiou (1980) state that such a configuration, which involves the protogalaxy already being present within the protohalo, is not possible under the hierarchical structure formation model of ΛCDM. For these reasons, we focus our attention on the latter model.

1.2.3 Spherical Collapse Model

The following results are given from the Lund University course `ASTM27`. Under the ΛCDM model, the nature of halo structure formation is hierarchical and bottom-up, where large halos contain smaller satellite halos. When looking at the halos themselves, they are predicted to be objects that are dominated by self-gravity. This is the basis of the spherical collapse model of DM halos. Under their self-gravity the DM of the universe forms into spheres.

This model describes regions of over-density where $\Omega_{m,0} = 1 + \Delta$ is slightly higher than the background density of the universe. This over-density leads to DM caving into itself, and under the assumptions of this model, the collapse is described as a "mini-universe" decoupled from the background, which behaves as a closed and matter only system. The cycloid solutions can be determined from the following differential equation characterizing the collapse, assuming $\Delta \gtrsim 1$:

$$\left(\frac{dR}{dt}\right)^2 = R_0^2 H_0^2 \left[\Omega_{m,0}\left(\frac{R_0}{R} - 1\right) + 1\right]$$

The assumption on Δ places the problem in the non-linear regime and physically translates to a model in which the DM on small scales collapse first, and the linearity of the large scale structures are unaffected by the perturbations.

Analytical solutions to the above equation exist for the radius R and the time t. The over-density will initially expand with the universe and reach a maximum size at t_{max} and $\theta = \pi$. Once this maximum is reached, it will collapse into a singularity and reach $R = 0$ at $\theta = 2\pi$. Expressions for the turnaround radius, defined to be where the perturbations reach the maximum size ($\theta = \pi$) and over-density can be obtained using the Friedmann equation (Mo et al., 2010a).

This gives an over-density of $\dfrac{\rho}{\rho_0} \approx 5.55$ at turnaround and $\dfrac{\rho}{\rho_0} \to \infty$ at collapse. ρ_0 is the background density of the universe. However, DM halos are expected to exist in an equilibrium in our universe, which establishes the concept of virialization. The Virial Theorem states the following.

Virial Theorem: The gravitational potential energy of a self-gravitating system in equilibrium is twice that of the kinetic energy of the system and is of opposite sign

$$E_{\mathrm{pot}} = -2E_{\mathrm{kin}}$$

In the context of the spherical collapse model, the time of virialization is $t_{\mathrm{vir}} = 2t_{\mathrm{max}}$, i.e., the time of collapse. It is therefore assumed that once the DM collapses it reaches an equilibrium state. From here it is possible to define the virial radius as a function of the turnaround radius, using the potential for a uniform sphere and equating the energy at the turnaround and at virialization.

From the virial theorem at the time of virialization, the over-density of a virialized sphere in the Einstein-de Sitter universe can be shown to be:

$$\frac{\rho(2t_{\mathrm{max}})}{\rho_0(2t_{\mathrm{max}})} \approx 178$$

In this way, the collapse is described by non-linearity, and under these solutions the over-density at the turnaround is $\frac{\rho}{\rho_0} = 5.55$. The critical density threshold $\delta_c = 1.686$ however describes the extrapolated density at the time of collapse had the linear regime been extrapolated. Moreover, the non-linear solutions would have the DM halo collapse into a single point and this is addressed through the virialization of the DM halos. This description of DM halos is simplified and the cosmological zoom-in simulation codes use more robust numerical techniques to produce more accurate results.

In the literature, it is common to define the virial density where a virialized over-density of 200 is assumed (~ 178). In this case, the virial radius R_{200} is defined as the radius such that the enclosed sphere has mean density 200 times that of the critical density of the universe. The virial mass M_{200} is then the mass enclosed within the virial radius R_{200}.

We can also define the very useful quantity ρ_{crit}, which is the critical density of the universe and which is used as the reference point when computing the virial quantities. From here is defined the virial radius and virial mass, quantities that are commonly used to describe the DM halos.

As described above, in our work we will define the virial boundary to be the point in which the enclosed sphere has mean density 200 times that of the critical density of the universe and this will be used to compute the virial properties of the central halo and subhalos.

1.2.4 Angular Momentum

Let us introduce several concepts regarding angular momentum in the context of galactic dynamics.

Let us first consider a gravitating and isolated system of N particles. We can define the total angular momentum of this system as the sum total of each particles angular momentum (Binney & Tremaine, 2008). This gives the following formula:

$$\mathbf{J} = \sum_{i}^{N} m_i \mathbf{r}_i \times \mathbf{v_i}$$

where m_i, $\mathbf{r}_i$ and $\mathbf{v}_i$ are respectively the mass, position and the velocity of the ith particle in the system.

From this can be defined the specific angular momentum $\mathbf{j}$, which is simply the angular momentum per unit mass (Binney & Tremaine, 2008). This is given as:

$$\mathbf{j} = \frac{\mathbf{J}}{M}$$

where M is the total mass of the system.

In the context of galactic dynamics, angular momentum plays an important role in its formation and evolution (Stewart et al., 2013). The question around its origin in DM halos and their host galaxies remains a topic of discussion and debate. Our current understanding of DM halo formation and the description of angular momentum emergence and evolution is built on several theories. A core theory in the literature regarding the origin of angular momentum is Tidal Torque Theory (TTT). First formulated by White (1984), it was built on the works of F.Hoyle (*Problems of Cosmical Aerodynamics*, Paris 1949) and Peebles. Hoyle first proposed the idea that the angular momentum acquired by protogalaxies was a result of tidal torques initiated by gravitational instabilities arising from neighbouring perturbations. He assumed that the proto-galactic cloud was not uniform and that during condensation - the mechanism behind the collapse and formation of a galaxy - it would acquire angular momentum. However, he also mentioned that external gravitational fields would further contribute to AM generation, identifying such externalities as possible

Figure 1.4: Simulated binary pair of DM halos where the small white dots are subhalos to the two main DM halos from Moore (2001)

other proto-galaxies or irregularities in the distribution of the internebular material. Moreover, Hoyle noted that these newly formed protogalaxies produce further irregularities in the intergalactic medium due to their peculiar motion within it, leading to overdensities and underdensities via gravitational effects and forming more proto-galaxies.

Peebles (1969) reframed Hoyle's ideas in the gravitational instability framework and provided quantitative results which demonstrated the compatibility of both theories. He found that gravitational forces, within an order of magnitude, could account for the angular momentum computed in our galaxy. He later defined the dimensionless spin parameter λ in Peebles (1971).

The galactic spin parameter λ can be defined to help characterize DM halo dynamics. The galactic spin parameter is a dimensionless parameter of the galactic halo which measure the importance of rotation relative to gravity. It has the following equation (Binney & Tremaine, 2008): $\lambda = \frac{J\sqrt{|E|}}{GM^{\frac{5}{2}}}$ The galactic spin parameter can also be written in another form (Yang et al. (2023);Bullock et al. (2001)): $\lambda = \frac{j}{\sqrt{2}V_{200}R_{200}}$ where j_h is the specific angular momentum, R_{200} is the virial radius and M_{200} is the virial mass.

Crucial in Peebles's paper is the assumption that the proto-galactic region was completely spherical and symmetric. The geometry of such a system led him to conclude under perturbation theory that the first-order terms disappear and angular momentum grows to second order. In the years following, it was shown that AM does indeed grow at first order. Using the Zel'dovich approximation (Zel'dovich, 1970) as a Lagrangian framework for tracking particle displacements, Doroshkevich (1970) found that for a triaxial - and therefore non-spherical - proto-galactic density distribution, the AM grew at first order and evolved faster than what was previously predicted by Peebles (1969).

In White (1984), the model was improved and the foundational result of TTT - that AM arises from a misalignment of the tidal and inertia tensors in the linear regime - was introduced. Moreover, he described the end of momentum acquisition at turnaround, which effectively delineates the linear and non-linear regimes. This was confirmed in several N-body simulations he conducted which followed both regimes and showed that non-linear collapse led to AM conservation rather than generation.

While TTT is a well-established theory in the literature, it is incomplete and fails to answer certain fundamental questions. For example, Porciani et al. (2002a) showed that the spin amplitudes of today's proto-halos match the TTT predictions only if the growth is assumed to stop after 55-70% of the turnaround time. Moreover, Porciani et al. (2002b) showed that while TTT predictions for angular momentum are statistically consistent when compared against N-body simulation results averaged over several thousands of haloes, there exist considerable deviations at the level of individual haloes, with scatter comparable in magnitude to the signal itself. This is a consequence of the near-alignment between the inertia and tidal tensors found by Porciani et al. (2002b): the principal axes of the two tensors are strongly aligned, such that the angular momentum - arising as a residual of this near-cancellation - is highly sensitive to small errors in the individual tensor estimates.

Alternative models have therefore been proposed to account for TTT's limitations at the individual halo level. Vitvitska et al. (2002) proposed that dark matter haloes acquire their angular momentum primarily through the cumulative orbital angular momentum contributed by successive mergers with satellite haloes. In this framework, each merger event adds an increment of angular momentum determined by the orbital parameters of the infalling satellite, such that the total halo spin evolves as a random walk over the halo's merger history. Tidal torques are not abandoned in this picture but reframed - rather than torquing the proto-halo directly, they establish the initial orbital velocities of infalling satellites, whose angular momentum is then transferred to the host halo upon merging.

However, Cadiou et al. (2021) demonstrated that angular momentum evolution within fixed Lagrangian patches can be predicted 2-4 times more accurately than TTT alone, by replacing the theoretical TTT growth rate with the growth rate measured from a reference simulation. Crucially, this result suggests that angular momentum evolution is not driven by chaotic or stochastic processes, but is instead a deterministic consequence of the initial conditions. The authors attributed the remaining inaccuracies of TTT to the ambiguity in defining halo boundaries, rather than to non-linear evolution itself.

In recent years, as our understanding of angular momentum acquisition has developed, some interest has been directed towards subhaloes. Boylan-Kolchin et al. (2008) characterised the orbital parameters of subhaloes at infall in ΛCDM simulations and found circularities broadly peaking around $\varepsilon \approx 0.5$, indicating that most satellites follow moderately eccentric orbits rather than purely radial or circular ones. Here, the orbital circularity is defined as $\varepsilon = L/L_c(E)$ - the ratio of a satellite's angular momentum to that of a circular orbit of the same energy - such that $\varepsilon = 0$ corresponds to a purely radial orbit and $\varepsilon = 1$ to a purely circular one. This distribution of orbital circularities is not arbitrary - it is set by the angular momentum structure of the large-scale environment from which satellites are accreted. The angular momentum of the host halo, acquired through the tidal torque mechanism described above, is correlated with the surrounding cosmic web geometry (Codis et al., 2015), which in turn determines the directions from which satellites are accreted and therefore the distribution of their orbital circularities at infall. The spin of the host halo therefore has consequences that extend beyond its own internal structure to influence the orbital properties of its satellite population. Furthermore, studies of angular momentum conservation within DMO simulations have revealed that on an individual particle level, angular momentum is not strictly conserved, with variations across radial shells of order a factor of three Book et al. (2011), highlighting the complexity of angular momentum evolution beyond the simplified assumptions of analytical models.

1.3 Project Goals

The central aim of this thesis is to determine how modifying the initial angular momentum of a Milky Way-like dark matter halo affects the orbital and structural properties - in particular the specific orbital AM, virial radius, virial mass, and radial distance to the central halo - of its satellite subhalos, using the novel DMO VINTERGATAN-GM-AM simulation suite. In doing so, we also develop a methodology for cross-identifying the same subhalo across genetically modified simulation runs.
As discussed previously, we have worked with DMO simulations which have provided us with results which completely isolate the gravitational role of angular momentum and removes the effects of baryonic physics such as feedback processes, star formation and gas physics on the dynamics of the subhalos. Indeed, the impact of these processes are not under investigation in this project, and their presence would lead to degeneracies, making it more difficult to identify the effects of angular momentum. By removing baryons from the simulation, we are able to more accurately determine the fundamental role of angular momentum. We presented the context and theory around the field of galaxy formation and evolution in sect.1, as well as discussed the current standard model of the universe - λCDM model - and DM halos as well as provided a short literature review regarding the research on the effect of angular momentum on galaxy mergers. In Sect. 2.4, we describe the different tools we used for the analysis, including the data analysis python library `YT` and the halo finder `ROCKSTAR`. Moreover, we discuss the theory behind halo finding as well as introduce the different codes used in the VINTERGATAN-GM-AM simulation, including the initial condition generator `genetIC` and the code on which the simulations were run `RAMSES`. For the former code, we explain the approach that was used to modify the AM in the simulations. We present our findings in chapter 3, where we have looked at four properties of the subhalos to analyze - specific orbital AM, viral radius, virial mass and radial distance to the central halo. Finally, in chapter 4 we discuss our findings and relate it back to the what is available in the literature today, before outlining in detail the limitations of our work as well as the outlook for future projects.

Chapter 2

Methodology

In this chapter we describe the tools, codes, simulations, and analysis methods used to address the central research question. We provide background on the Python library YT and halo finders, in particular ROCKSTAR, which were used to extract and examine the data. We then detail the technique employed using genetIC to generate the suite of simulations with the desired AM modifications, before introducing the RAMSES code on which the simulations were run and the VINTERGATAN−GM−AM simulation suite itself. Finally, we describe the methods used to identify and track subhalos across simulation runs, which form the basis of the analysis and results presented in Chapter 3.

2.1 Tools for Analysis

2.1.1 YT

In order to interact with, analyze, and visualize, we used the open-source python library YT (Turk et al., 2011). Although this package was initially designed to process astrophysical data, it is used in many other fields such as seismology, nuclear physics, and oceanography, to name a few. Its flexibility allows for exploratory research, especially in large scale simulations such as the ones we have worked with. In fact, YT was first designed as an analysis tool for the ENZO simulation code and was further developed to handle other codes such as RAMSES. This cross-code implementation allows for comparison between simulations and verification of results between research groups.

YT is particularly interesting for exploratory research due to its flexibility and adaptability. Indeed, the python package has built-in fields of astrophysical quantities that can be extended through post-processed derived fields. As defined by the user, these fields can either be defined using the raw data of the simulation or the built-in YT fields.

Additionally, its versatility proved important for comparing the different simulation suites. Having a single data analysis tool kit leaves less room for error and allows for more faithful comparisons to be conducted. The results are also more reliable due to the collaborative nature of the project and has been used quite substantially in the literature.

One reason it is used is its efficient handling of large data-sets which are ever present in astrophysical cosmological simulations. Indeed, YT uses parallelization through Message Passing Interface (MPI)(Dalcín

et al., 2005), a feature which is directly integrated in the package. This paralleization was used to run the `ROCKSTAR` halo finder.
`YT` is also used to run the halo finders that we will discuss in 2.1.2 and extensions can be downloaded to do further analysis on them. It is therefore a multi-purpose tool that allows us to directly interact with the data in-depth. In the scope of this project, the aforementioned flexibility of the package, along with its efficient handling of large datasets from multiple different codes was important as it allowed for ease in managing and working with the VINTERGATAN simulation suites data where the emphasis was placed on the investigation of different astrophysical quantities. Moreover, the integration of unit and dimensional analysis tools in the package through `unyt` (Goldbaum et al., 2018) - a python library developed for the `YT` project to introduce physical units during the processing of the data - allowed for easy conversion between units, which was particularly useful given the contrasting units used by `ROCKSTAR` and the simulation codes.

2.1.2 Halo Finding

2.1.2.1 Halo Finders

An integral part of the project was the detection and analysis of the DM satellites around the main halo. While the identification of DM halos can seem rather trivial at first glance, it proves to be quite challenging and different strategies have been developed to perform this task. Different codes will detect slightly different subhalos. Indeed, each halo finder will have different definitions for what constitutes a subhalo. Moreover, the merging and interactions between the subhalos with their halo further complicate the process of properly defining and detecting the former, and leads to the added difficulty of hierarchical grouping of DM particle clusters. In the literature, two categories of halo finders can be defined: density peak locator and particle collection halo finders (Knebe et al., 2011).
The density peak locator halo finders such as the spherical over-density (SO) halo finders use the density profile of the DM clusters in order to determine their central point. The regions of high matter density are first detected in the computational domain. The DM cluster centres are defined and the density profile is constructed outward. A density lower limit is set which defines the boundary of the DM halo. This is often defined to be the virialization threshold defined by the spherical collapse model.
An example of this procedure is present in certain SO halo finders and is done as follows. The density is defined for each particle by choosing a user-defined number of particles N around it, and defining r_N the distance to the furthest of these N particles from the particle of interest. The density is thus

$$\rho = \frac{N}{\frac{4}{3}\pi r_N^3}$$

In each region the particle with the highest such density is selected as the halo center. A sphere is then constructed and outwardly grown until the mean density that is enclosed in the sphere meets a minimum predefined over-density threshold, at which the halo boundary defined. The particles within the halo boundary is assigned to this halo and the process is continually repeated on other density peaks. A pruning process is often common in order to remove particles that are unbound and therefore no gravitationally associated to the halo when computing halo properties.
The alternative method is through particle collection. One uses the geometry of the particles to link them

together using their 6D-phase space properties. These methods employ a Friends-of-Friends (FOF) algorithm (Davis et al., 1985), in which a linking length is defined. The linking length is the distance such that any two particles found separated by less than that are linked together. Both the particle positions and the particle velocities are used to construct the subhalos. This is particularly interesting with regards to the tracking of halos across multiple snapshots as this removes the degeneracy that may occur during interactions of halos, such as is the case when a subhalo passes through the main halo. In this context, the subhalo particles would move in a direction and at speeds that are distinct from the main halo.

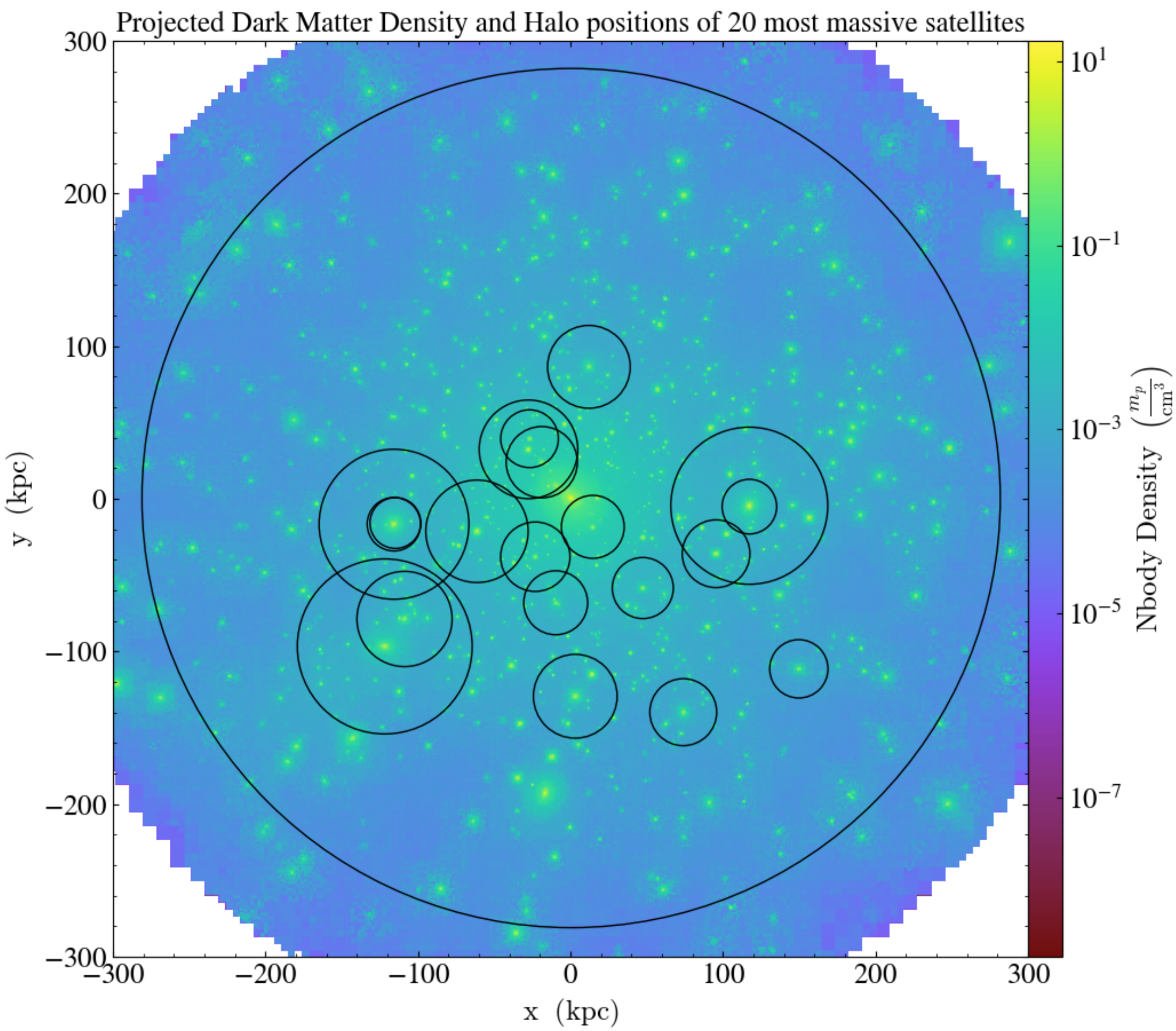

Figure 2.1: Example of Halo Idenfication using ROCKSTAR (the circles define the virial radius of each subhalo)

2.1.2.2 ROCKSTAR

In this project we used ROCKSTAR, a particle collection halo finder which uses an FOF algorithm developed in 2010 by Behroozi et al. (2013) with an emphasis on improving the accuracy of merger tree construction. Indeed, in order to analyze the subhalos, it is crucial to be able to track them in time and to get a very precise understanding of its merger history. Moreover, ROCKSTAR's implementation within the YT framework facilitated its application and justified its usage. A final consideration was the halo finder's ability to run on very large data sets such as the one's we were working with. Notably, ROCKSTAR was built to be very robust with high resolution cosmological simulations in mind, and uses efficient parallelization in its algorithms. It was tested on multiple simulation datasets involving more than 10^{10} particles such as the Bolshoi simulations (Klypin et al., 2011). We have shown in Fig. 2.1 an example of a halo identification we performed using ROCKSTAR, where we have identified the 20 most massive satellites in the zoom-in region of the simulation.
As stated above, ROCKSTAR uses a FOF algorithm. Its implementation is slightly more involved than other halo finders using the same approach. A rapid variant of the 3D FOF method is first used to determine the over-dense regions. In ROCKSTAR the linking length, which is used to preliminarily find these clusters is defined as a fraction b of the mean interparticle distance, which is itself the cube root of the mean particle volume. The most commonly used value for the free parameter b in the literature is 0.2 (More et al., 2011). This value $b = 0.2$ is significant as Jenkins et al. (2001) found the mass function to be universal under all cosmologies. Nevertheless, it is also common to see $b = 1.0$ and $b = 1.5$ (White, 2001).
In order to confidently determine the virial spherical over-densities for DM halos of all morphologies, including the most extreme ellipsoids, Behroozi et al. (2013) found that a linking length $b = 0.28$ was optimal. The commonly used value of 0.2 fails to include all the particles in the virial radius of the DM halo.

2.2 Codes

2.2.1 genetIC

The VINTERGATAN-GM-AM, which will be discussed further in sect.2.3.1, uses genetIC (Stopyra et al., 2021) to apply the modifications to the different angular momentum scenarios. Indeed, genetIC is a code which generates initial conditions for cosmological n-body simulations. The code allows users to specify modifications to diverse parameters such as the merger history, mass, angular momentum and environmental factors. It is particularly interesting as it is adapted for cosmological zoom-in simulations, such as VINTERGATAN-GM-AM.
This method of generating data is efficient due to its targeted nature, instead of running many more simulations in order to get a statistically significant result.
The code first generates a gaussian random field as its initial density field for the universe - a normal distribution in N^3 dimensions, where N is the number of grid cells along one side of the simulation box. For such a distribution, there exists an analytical exact solution to the problem of drawing a field conditioned on a given constraint (Hoffman & Ribak, 1991), which genetIC implements efficiently through a series of mathematical optimisations. The algorithm first locates the particles of interest that need to be changed and minimizes the number of modifications it has to perform to satisfy the constraints of the modified

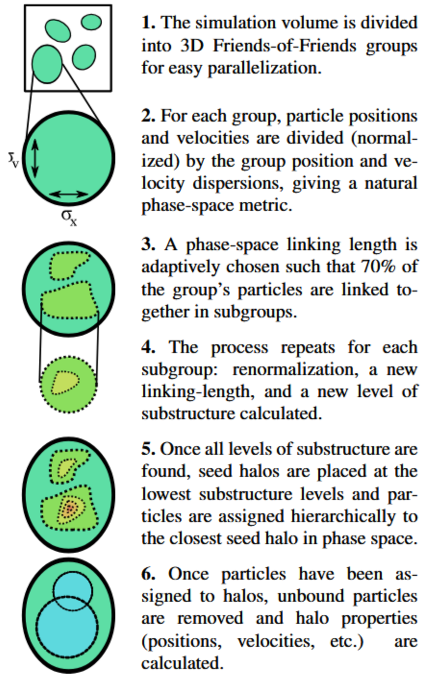

Figure 2.2: A visual summary of the FOF algorithm implemented by ROCKSTAR (Behroozi et al., 2013)

initial conditions. By limiting the modifications that need to be done, the GM simulations remain as close to the fiducial simulation as possible. Once the modifications are made and the power spectrum is generated, other fields can be obtained by solving the different astrophysical equations. The process for generating the initial condition fields is presented in Fig. 2.3.

More specifically, let us provide a qualitative explanation of its implementation in the VINTERGATAN-GM-AM simulation suites refering to Cadiou et al. (2021).

The simulation box can be decomposed into cells. For a given field **f**, each cell is assigned a value or values. In the simulation box, a smaller fixed lagrangian patch Γ is defined. Γ is determined by identifying the particles of the main halo at $z = 0$ in the fiducial run and tracing back the region that contains them at $z = 99$. It is therefore the region in the initial condition that contains all the particles of the main halo in the final snapshot. It is important to note that the region is defined based on particle membership and not spatial boundaries. Indeed, between simulations, if Γ was drawn out to include all the particles, the regions would look different due to the slight displacements made between runs to satisfy the AM modification condition.

Let us define f_0 to be initial density field. Moreover, let **u** be a linear function which takes as input a field f_0 and outputs a scalar value d. We can define the following operation:

$$\mathbf{u} \cdot \mathbf{f} = d$$

where **f** is an N^3-dimensional vector, where N is the number of grid cells along one side in the simulation box, **u** is a $1 \times N^3$ matrix and d is a scalar value. In practice, the above operation is applied on the gravitational potential field and the scalar output is the angular momentum in each cartesian direction.

More specifically there exist three separate linear mappings $\mathbf{u}$ defined for each direction x, y, z. We therefore get the following expressions:

$$\mathbf{u}_x \cdot \mathbf{f}_{0,i} = l_{\mathrm{x,0,i}}$$

$$\mathbf{u}_y \cdot \mathbf{f}_{0,i} = l_{\mathrm{y,0,i}}$$

$$\mathbf{u}_z \cdot \mathbf{f}_{0,i} = l_{\mathrm{z,0,i}}$$

where i is the merger scenario under consideration.

The AM that is desired is known, however the linear operators $\mathbf{u}_{x,y,z}$ are not. The fields $\mathbf{f}$ is what the `GENETIC` code solves for. It is therefore relevant to determine the linear operators $\mathbf{u}_{x,y,z}$. To construct u, one proceeds through a chain of linear operations: the density field δ is first used to solve Poisson's equation in Fourier space to obtain the gravitational potential Φ; its gradient $\nabla\Phi$ is then computed; and finally the torque integral over Γ is evaluated. This chain is exact at sufficiently high redshift, before shell crossing occurs, making it valid at z = 99.

This was done by taking the density field and solving the Poisson equation in fourier space to obtain the reduced potential field. As demonstrated in Cadiou et al. (2021), from the integral equation of the initial value of the specific AM, the value of angular momentum in each direction is given by:

$$l_{x,0} \propto \sum_j [(q_y^{(j)} - \bar{q}_y)\nabla_z \phi^{(j)} - (q_z^{(j)} - \bar{q}_z)\nabla_y \phi^{(j)}]$$

$$l_{y,0} \propto \sum_j [(q_z^{(j)} - \bar{q}_z)\nabla_x \phi^{(j)} - (q_x^{(j)} - \bar{q}_x)\nabla_z \phi^{(j)}]$$

$$l_{z,0} \propto \sum_j [(q_x^{(j)} - \bar{q}_x)\nabla_y \phi^{(j)} - (q_y^{(j)} - \bar{q}_y)\nabla_x \phi^{(j)}]$$

where $\bar{q}$ is the center of mass of the lagrangian patch Γ and defines a reference point from which the AM is computed. Moreover, the sum is taken over all cells in Γ. The position of each cell is given in lagrangian coordinates denoted as q.

The gradient components $\nabla_{x,y,z}\phi^{(i)}$ are then multiplied by the corresponding lever arm $(q^{(i)} - \bar{q})$ of cell i relative to the patch centre of mass - these define the term of the linear operator at that grid. The resulting contributions are summed over all cells. From this we retrieve the discrete angular momentum formulae defined previously.

The elements of the linear operator can be thought of as weights given to the gravitational potential value at each cell.

The full operator is then assembled by summing over all cells (i,j) in Γ.

$$\mathbf{u}_z \cdot \mathbf{f} = \sum_{(i,j)\,\in\,\Gamma} \Delta u_z^{(i,j)} \cdot \mathbf{f}$$

Given the operator u and the original field f, the modified field f' satisfying the new constraint $\mathbf{u} \cdot \mathbf{f'} = d'$ is found via χ^2 minimisation of $(\mathbf{f'} - \mathbf{f})^\top \mathbf{C}^{-1}(\mathbf{f'} - \mathbf{f})$, where C is the covariance matrix of the Gaussian random field. This yields the unique solution closest to the original field under the metric defined by $\mathbf{C}^{-1}$, and can be written analytically as $\mathbf{f'} = \mathbf{f} + \frac{(d' - \mathbf{u} \cdot \mathbf{f})\mathbf{Cu}}{(\mathbf{u}^\dagger \mathbf{Cu})}$ (Hoffman & Ribak, 1991)

The uniqueness comes from the minimization and the field associated to the specific AM modification that

is made is found. For the VINTERGATAN-GM-AM suite specifically, the operator u was first applied to the fiducial field to obtain the reference AM $d_0 = \mathbf{u} \cdot \delta$, and the five runs were then generated by targeting $d' \in \{0.5\, d_0,\ 1.05\, d_0,\ 1.1\, d_0,\ 1.2\, d_0,\ 2.0\, d_0\}$. These changes between the VINTERGATAN-GM-AM suite of runs are reflected in the changes between the particle velocity magnitudes as shown in Fig. 2.5. Here we have zoomed in on the host halo region and show results for the $AM_{fid} \times 0.5$ and $AM_{fid} \times 2.0$ runs, as these two extremes in our initial AM momentum display the most pronounced differences.
An example of its usage is in the VINTERGATAN-GM suite of simulations conducted in Joshi et al. (2024). In this paper, a genetically modified version of VINTERGATAN was run in which the initial mass of a MW-like halo was modified. 5 different scenarios were created with a major merger occurring at around $z \sim 2$. Moreover, the genetic modification was initialized such that in each simulation scenario, the halo has the same mass at $z = 0$. An example of how the genetic modification applies specific changes to a zoom-in simulation is given in Fig. 2.4.
The genetic modification technique is therefore very effective in isolating the effects of a parameter - in our case the angular momentum - and exploring the impacts of this parameter on the evolution of the halo and its satellites while keeping the other properties of the simulation as close to the fiducial run as possible.

2.2.2 RAMSES

RAMSES (Teyssier, 2002) is an N-body and hydrodynamical simulation code that uses an oct-tree based Adaptive Mesh Refinement (AMR) framework. It was developed in 2001 to study structure formation in astrophysical systems. Its high spatial resolution is a consequence of its AMR algorithm, which implements a tree based data structure to refine the grids in locally more dense regions of the simulation box. It is therefore a very suitable code on which to run large cosmological zoom-in simulations on pc to Mpc scales. In RAMSES, simulations lie on a cartesian grid on which which is recursively refined locally in the densest regions. Moreover, it solves the Vlasov-Poisson equations which describes the collisionless N-body system of the DM particles and uses a hydrodynamical solver based on a second-order Godunov method in order to resolve the conservative form of the governing Euler equations on mass, momentum and energy conservation.

$$\frac{d\mathbf{x}_p}{dt} = \mathbf{v}_p \text{ and } \frac{d\mathbf{v}_p}{dt} = -\nabla_x \phi \text{ where } \Delta_x \phi = 4\pi G\rho$$
$$\frac{\partial \rho}{\partial t} + \nabla \cdot (\rho \mathbf{u}) = 0$$
$$\frac{\partial}{\partial t}(\rho \mathbf{u}) + \nabla \cdot (\rho \mathbf{u} \otimes \mathbf{u}) + \nabla p = -\rho \nabla \phi$$
$$\frac{\partial}{\partial t}(\rho e) + \nabla \cdot [\rho \mathbf{u}(e + \frac{p}{\rho})] = -\rho \mathbf{u} \cdot \nabla \phi$$

The above equations are the Vlasov-Poisson and Euler equations solved by RAMSES where p refers to the particles in the n-body framework.
In this thesis the VINTERGATAN-GM-AM simulation suite uses the RAMSES code. The simulation code is continually updated, and therefore a more modern version of RAMSES, with improved contemporary physics and computational efficiency, was used to perform the simulations. Note that the simulations we worked on in this project are DMO simulations, therefore the hydrodynamical equations are not applicable.

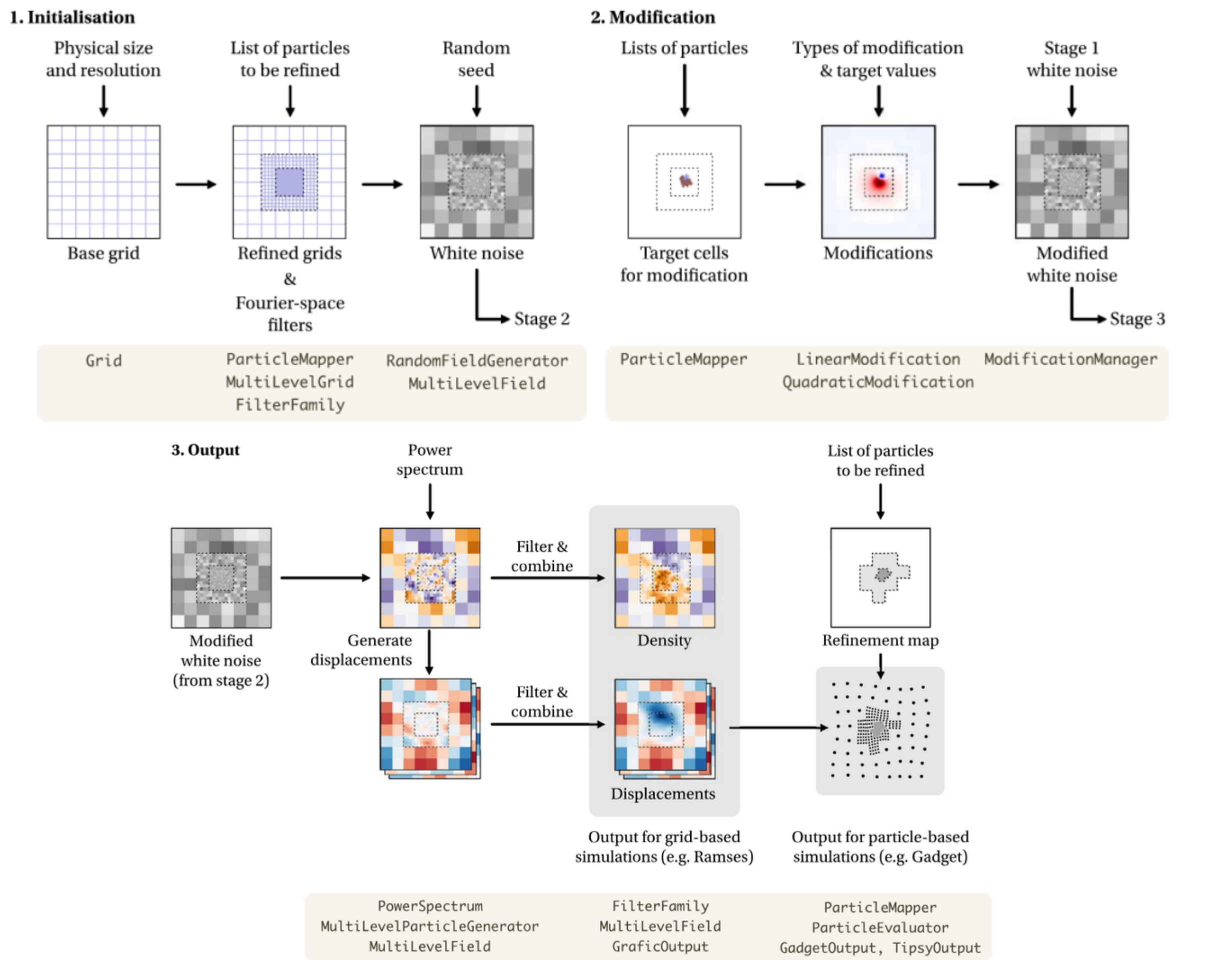

Figure 2.3: A visual summary of the genetic modification algorithm implemented by genetIC (Stopyra et al., 2021)

2.3 Simulation

2.3.1 VINTERGATAN-GM-AM

The set of simulation suites used for the analysis in this project is the VINTERGATAN-GM-AM suite of simulations. This suite of simulations builds on the VINTERGATAN simulations which study the formation of MW-mass galaxies. The simulations we have analyzed in our project uses a genetically modified version of these simulations. Indeed, one can investigate the effect that modifying a parameter such as the initial mass or merger timing of progenitor galaxies will have on the emergent galaxies. This is implemented by performing controlled changes to the initial conditions. By doing so, we create several scenarios concerning the same galaxy, that vary slightly in their cosmological histories, without any changes to the large scale structures of the simulation.

In the scope of this project, the main parameter that we analyzed was the effect that modifying the angular momentum of progenitor galaxies has on the satellite properties of the emergent galaxy. The simulations

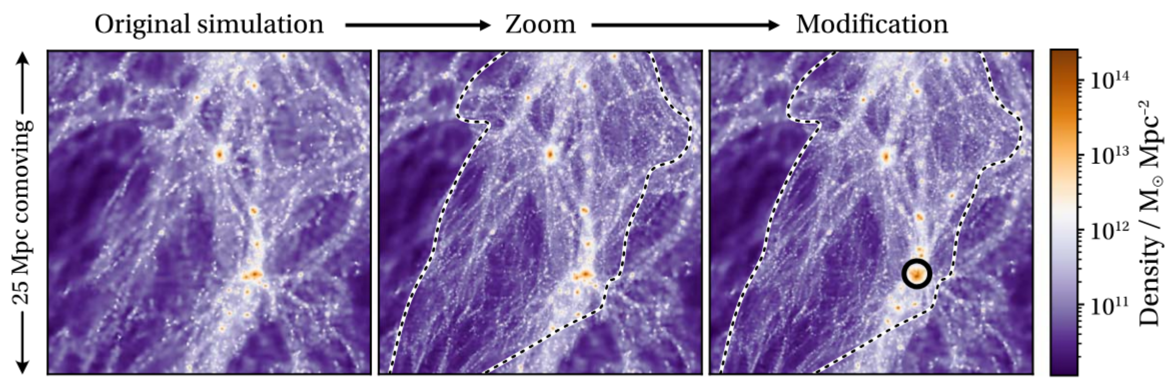

Figure 2.4: A visual example of a genetic modification(20% increase of initial density) being applied on a DM halo. Some small halos may be present in the fiducial plot but not on the modification plot and vice versa due to movements perpendicular to the page)(Stopyra et al., 2021)

that we have worked with to perform this comparison project was initially run by Corentin Cadiou with the following cosmological parameters found in the T. 2.1. Between the initialisation time at $z = 99$ and the end there are a total of 101 snaphsots. Moreover, the simulation data we worked with were the DMO runs. We therefore do not consider the baryonic physics involved in the mergers. Physical processes such as gas cooling, stellar feedback, supernovae and Active Galactic Nuclei (AGN) are therefore not considered in these simulations.

Table 2.1: Summary of VINTERGATAN-GM-AM simulation parameters

Parameter	5 Runs
Box size (Mpccm)	74
Particle mass ($M_\odot$)	1.2×10^5
$H_0(\frac{km.s^{-1}}{Mpc})$	0.672
Particle mass ($M_\odot$)	1.2×10^5
Ω_λ	0.686
Ω_m	0.314
Ω_k	0.501
Ω_b	0.0
z_{init}	99
z_{final}	0
N_{DM}	27752047

`genetIC` was used to modify the initial conditions of the different simulations. In the suite of simulations that we analysed in our project, the main galaxy was first identified in the high resolution zoomed-in region at redshift $z = 1$. Its two main progenitors - the most massive - and their particles were then selected. The latter were tracked to their initial conditions. The gravitational torque of these particles were then modified on five different occasions to create the five different runs of the simulation suite. Since the gravitational torque is responsible for angular momentum generation in the linear regime, its modification effectively results in different angular momentum amplitude and evolution in the main galaxy.
The changes made in the different simulation runs are defined relative to the fiducial iteration. Only the

relative changes in angular momentum between simulations is interesting to us. The gravitational torques of the different runs in our analysis are scaled with respect to that of the fiducial simulation by a factor of $\{0.5, 1.05, 1.1, 1.2, 2\}$.

Before proceeding to the analysis, it is worth stating the key assumptions and limitations that shape the scope of the research as well as the interpretation that follows. Below we have enumerated the most important. The implications of these points are discussed further in Section Sect. 4.2.

1. The simulated data are DMO (baryonic processes such as gas cooling, stellar feedback, supernovae, AGN, etc. are absent). This is a deliberate choice to isolate the purely gravitational role of AM, but means the results do not capture the full complexity of galaxy formation.
2. Halos are defined using the virial overdensity criterion $\Delta = 200\rho_{\rm crit}$; the choice of threshold affects the measured virial radius and mass.
3. Only 3 subhalos from a single host halo are analyzed, limiting the statistical generality of the results.
4. All five runs share the same large-scale environment (only the AM is modified).
5. The subhalo sample is biased towards objects that have not undergone major mergers or collision, as the method which is described in Sect. 2.4 used to identify and track them favors subhalos with particle membership that is stable across all runs and snapshots.
6. The numerical resolution may be too low to reliably track properties of heavily tidally stripped subhalos at low redshift.

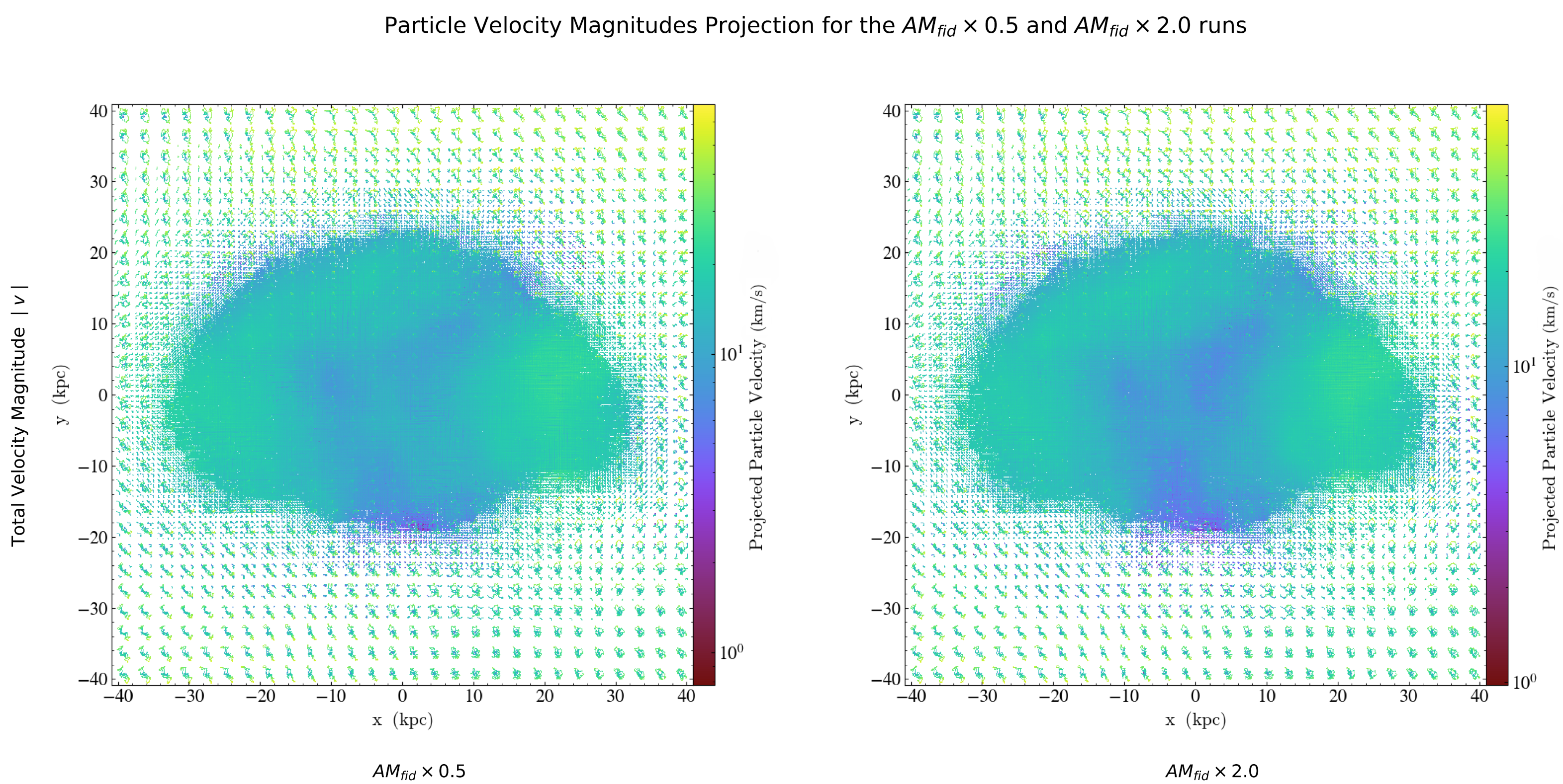

Figure 2.5: Particle velocity magnitude at z=99 for the $AM_{fid} \times 0.5$ and $AM_{fid} \times 2.0$ DMO simulation runs. The subtle differences visible between runs reflect the modifications to the initial conditions introduced by the genetic modification of the angular momentum.

2.4 Methods

In this thesis, we worked with novel DMO VINTERGATAN-GM-AM simulated data of a MW-like galaxy, in which five merger scenarios are investigated where the free parameter that is modified for each simulation is the angular momentum. The simulations use `genetIC` to modify the initial conditions of each simulation to reliably observe the effects that modifying the angular momentum has on the halo dynamics (as discussed in Sect.2.2.1).
We first identified the high resolution region and the main halo by locating the region with the minimum cell volume. This indicates the region of highest resolution in the cosmological zoom in simulation, and therefore provides the general location of the main halo.
In our analysis it is important to consider the main halo and its properties as they will later be used to determine certain subhalo properties. Indeed, the motivation behind extracting accurate information central halo is in the effort to obtain the most reliable data on how our different subhalos properties evolve in time. These properties, such as the orbital angular momentum for a subhalo, rely on main halo quantities including its centre, mass and velocity. While `ROCKSTAR` computes certain characteristic quantities such as these, it can often be unreliable and it can be intellectually compelling to recompute.
Let us therefore focus our attention on the main halo. In order to have more reliable information on the main halo, we decided to recompute several quantities using the simulation data (ie. the DM particle information). More specifically, we decided to recompute the center of mass, virial radius, virial mass, and velocity.
We started by identifying the center of mass of the main halo. Having an accurate localization of the center of mass is crucial in order to accurately compute other properties of the main halo such as the virial radius. Furthermore, it is necessary for the later computation of the orbital angular momentum of the subhalos which uses the centre of the halo as the reference point.
The center was identified using an iterative shrinking sphere algorithm. While it was possible to compute it for snapshots above 15, those below gave unreliable results due to scattered particles as a result of incomplete clustering at early redshifts. The approach was to define a spherical region around an initial positional estimate and to compute the center of mass of the DM particles in the spherical region using the following equation:

$$x_{com} = \frac{\sum_i m_i \mathbf{x_i}}{\sum_i m_i}$$

where m_i and $\mathbf{x_i}$ are respectively the mass and positional vector of the each particle. At each iteration, this center of mass is computed and the sphere is redefined with this new center of mass as its center. Moreover, the sphere radius is reduced by a factor of 0.5, providing a progressive convergence towards the densest region in the DM halo. The stopping condition is defined such that if the sphere has radius less than $10kpccm$ or contains less than 100 particles, the iteration is terminated and the center of mass at that snapshot is computed. The latter condition is defined in order to compute the center at higher redshifts where some resolution problems were encountered when using `YT`'s units. This process is done in reverse chronological order, starting from the final snapshot, where the initial guess is taken to be the location of the minimum cell size, and the successive initial estimates are taken to be the center of mass computed previously in the above snapshot.
Having a precise center for each snapshot was important in order to compute the different properties of the

central halo.
One such quantity is the virial radius of the central halo. Knowing the virial radius of the central halo at each redshift is significant, as it is what defines the boundaries of the DM halo. It is therefore subsequently used to determine other properties such as the virial mass - which is integrated mass inside the sphere defined by the virial radius or simply the sum of the mass of the particles since we are working with discrete particles in our simulations. We used an iterative algorithm which involved defining a spherical region and comparing its DM density to the background density of the simulated universe. Indeed, in the literature the border of the virial radius is defined as the surface of the sphere where the average density inside is equal to $200\rho_{bkg}$. At each snapshot the background density of the universe was computed, and a spherical region was defined around the center of mass of the main halo at that snapshot.
This method also involved proceeding reverse chronological order of snapshots, such as in the algorithm to compute the center of mass, and the choice of the initial radius at the final snapshot of the spherical region was arbitrarily chosen to be the virial radius computed by `ROCKSTAR` $+100kpc$. Additionally, an initial step length is defined, which we arbitrarily chose to be $100kpc$. At each iteration, within a snapshot, the local density of the spherical region was computed and compared to the background density multiplied by a factor of 200 ($200\rho_{bkg}$), such that if it was larger than the spherical region was expanded by the corresponding step length and inversely if it was smaller. If two consecutive steps involved shrinking and expanding the sphere, the step length is modified to avoid loop errors and to converge to more refined estimate for the virial radius. The stopping condition is defined such that if the stepping length reaches below $1kpccm$, the iteration is terminated and the process is repeated for the next snapshot.
Interesting to note is the consideration that all particles in the spherical region belong to the main halo. Indeed, this assumption is justified by the size of the main halo compared to the subhalos - removing the particles in the subhalos from the main halo would have a negligeable effect. This practice is further seen in the literature such as in `ROCKSTAR`'s code Behroozi et al. (2013). The union of all particles in the main halo is taken. This goes against how the particle assignment is defined for subhalos, in which the union of particles excluding the intersection of such particles with the main halo in the subhalo virial radius is taken.
The virial radius defines the central halo. Once it is computed at each snapshot between 15 and 100, it was possible to compute the virial mass by taking the sum of all the particles in the sphere defined by the virial radius. Similarly, in order to compute the velocity of the main halo, we took the mean in each component of the velocity vector of all the particles inside the aforementioned sphere. Given the discrete nature of particles, the following formulas were used where we have only shown the computation of the x-component of the velocity without loss of generality.

$$M_{vir} = \sum_{i \in \mathcal{S}(r_{\rm vir})} m_i$$

$$V_x = \sum_{i \in \mathcal{S}(r_{\rm vir})} \frac{v_{x,i}}{N}$$

where N is the number of particles in the sphere $\mathcal{S}(r_{\rm vir})$ defined by the virial radius, m and v are the mass and velocity in x of each particle respectively, and the index i refers to the DM particles. It is interesting to note that in our simulation, every DM particle has the same mass, so the virial mass sum can be reduced to:

$$M_{vir} = Nm_{DM}$$

where m_{DM} is the mass of a DM particle.
In this project, we would like to compare how changing the angular momentum effects the properties of the satellite halos in the merger. It is therefore necessary to match the satellites in the different simulations, in order to be able to produce a one to one comparison of each halo in different simulation scenarios.
In an effort to cross compare the evolution of certain subhalo properties between merger scenarios, we identified 3 candidates to study. In order to determine these 3 subhalo candidates, a preliminary cross comparison algorithm was used. At the final snapshot, the 40 most massive subhalos were selected in each simulation. For each subhalo, a sphere with a fraction of the virial radius around its center was defined. The particles were then selected for each of the subhalos in each simulation. It is worth noting that the particle IDs between simulation runs is consistent. It is therefore possible to compare particles IDs between simulations. Using this, we selected one simulation run (we used the simulation run with relative gravitational torque 0.5 to the fiducial) and for each of the 20 most massive subhalos the particle IDs were cross compared to all of the particle IDs in every subhalo in each simulation. The objective was to see how many of the particles were identical and different, effectively heuristically determining as a first approximation which subhalos are equivalent between simulations(ie. composed of same particles). The following Jaccard similarity index was used to get the fraction of particles which were identical between two satellites:

$$J_{A,B} = \frac{N_A \cap N_B}{N_A \cup N_B}$$

where A and B are two different subhalos and N is the number of particles in the defined spherical region of each subhalo.
It is possible to do this cross comparison due to the initial make up of the cosmological simulation box, which places all the DM particles such that all the particles and their IDs are ordered in a consistent and identical manner across all simulation scenarios, and the gravitational clustering that occurs guarantees that the same particles will likely form the same subhalo. Collisions between subhalos can however lead to particles scattering, complicating this approach. A first group of subhalo pairs with Jaccard index above 0.1 is filtered through. Of these pairs, if there exists a degeneracy in a subhalo, the two with the closest virial radii are chosen using the follwing formula:

$$min(\frac{\mid R_{\mathrm{vir,A}} - R_{\mathrm{vir,B}} \mid}{R_{\mathrm{vir,A}}})$$

where A and B are two different subhalos and R is the virial radius.
With this we were able to find matches between all simulations of the same subhalo in the final snapshot. The three most promising set were taken and further analysis was done on them to properly match them. Indeed, what we have done above is show that the same particles in different simulations lead to the formation of similar subhalos at low redshift, however we would like to track each these subhalos across snapshots.
The following procedure was used to track the subhalos in time between each simulation.

1. The subhalo of interest is chosen and a spherical region is defined around its center with radius $0.05R_{vir}$
2. The IDs of the DM particles in sphere are extracted
3. For each merger scenario, the mean position and standard deviation of these particles is computed

4. The particles that deviate too far from the center are removed using the formula below
5. Once again, for each merger scenario the mean position of these new sets of particles is computed
6. The halos whose center is closest to these mean positions are selected from the `ROCKSTAR` catalogue of identified halos
7. At each snapshot, this method is repeated and one obtains for each merger scenario, the `ROCKSTAR` halo ID associated with the same particles

In step 4, the particles undergo a 2σ clip selection to the distribution, retaining those within two standard deviations of the mean.

$$\mid r_{\mathrm{x,y,z}} - \bar{r}_{\mathrm{x,y,z}} \mid < N\sigma_{x,y,z}$$

where $r_{\mathrm{x,y,z}}$ are the components of the positional arguments, $\sigma_{x,y,z}$ is the standard deviation in position in each direction of the particles and N an arbitrary factor, chosen to be $N = 2$ in our analysis.
Using the above method, 3 subhalos were selected for analysis which we will name subhalos 1,2 and 3.
Using the `ROCKSTAR` halo IDs identified using the above method, we were able to extract information on the subhalo properties at different snapshots and proceed with the analysis. Some of their properties at $z = 0$ are given in T. 2.2. The virial radius and the virial mass are directly given when running `ROCKSTAR` on all the snapshots of the simulation data. However, the radial distance and the specific orbital AM had to be derived from quantities computed by `ROCSKTAR`.

Table 2.2: Summary of the Subhalo Candidate Properties at z=0 in the $AM_{fid} \times 1.1$ Simulation Run

Subhalo	1	2	3
Virial Radius (kpc)	26.1	22.4	15.2
Virial Mass ($\times 10^8 M_\odot$)	9.79	6.30	2.32
$\mid j \mid$ ($\times 10^5 kpc\frac{km}{s}$)	5.32	7.88	5.44

The galactocentric radial distance of each subhalo was computed at each snapshot as the magnitude of the separation vector between the subhalo centre, as identified by `ROCKSTAR`, and the recomputed centre of mass of the main halo (as described above):

$$\mid r \mid = \sqrt{(x_{\mathrm{sub}} - x_{\mathrm{halo}})^2 + (y_{\mathrm{sub}} - y_{\mathrm{halo}})^2 + (z_{\mathrm{sub}} - z_{\mathrm{halo}})^2}$$

where $(x_{\mathrm{sub}}, y_{\mathrm{sub}}, z_{\mathrm{sub}})$ and $(x_{\mathrm{halo}}, y_{\mathrm{halo}}, z_{\mathrm{halo}})$ are the positions of the subhalo and the main halo centre respectively.
Similarly, the specific orbital AM of each subhalo was computed from the relative position and peculiar velocity vectors with respect to the central halo:

$$\mathbf{j} = \mathbf{r}_{\mathrm{rel}} \times \mathbf{v}_{\mathrm{rel}}$$

where $\mathbf{r}_{\mathrm{rel}} = \mathbf{r}_{\mathrm{sub}} - \mathbf{r}_{\mathrm{halo}}$ and $\mathbf{v}_{\mathrm{rel}} = \mathbf{v}_{\mathrm{sub}} - \mathbf{v}_{\mathrm{halo}}$ are the relative position and velocity vectors, respectively.

The magnitude of the specific orbital AM is then:

$$|\mathbf{j}| = \sqrt{j_x^2 + j_y^2 + j_z^2}$$

The tools, codes, simulation suite, and methods described in this chapter provides everything necessary to address the central research question. `YT` and `ROCKSTAR` allow us to extract the information regarding the central halo and its subhalos from the simulation data obtained via the `genetIC` and `RAMSES` codes. The methods outlined in Sect. 2.4 describe how we identified and tracked subhalos across all snapshots and simulation runs, ensuring that we are comparing equivalent objects across all five runs. It is under this framework that we proceeded to investigate and understand the impact of modifying the AM initial condition on subhalo properties. We present our findings in Chapter 3.

Chapter 3

Results

In this chapter we present the results of our analysis on the subhalos. In the following, we discuss the 5 different runs of simulation, each with the initial conditions on AM as described in Sect. 2.4, and we look into their effects on the subhalos we identified using the method outlined in Sect. 2.4. These results directly address the central aim of this thesis: understanding how modifying the initial AM of the host halo affects the properties of its satellite population. The chapter is divided into four subsections, each dedicated to a different property - specific orbital AM, virial radius, virial mass, and radial distance to the central halo. For clarity and succinctness we will denote each run $AM_{fid}\times\{0.5,1.05,1.1,1.2,2.0\}$ respectively. Additionally, at times we shall refer to $AM_{fid}\times1.1$ as the reference since we have used it as the baseline for all plots in which we have computed a relative difference. We have decided to plot the subhalos separately as we have very few subhalo candidates and any grouping of data would be statistically insignificant. As mentioned earlier, the main halo is not fully formed at the first snapshot and therefore it does not make sense to obtain information on its properties then. Certain characteristics of the subhalos depend heavily on these quantities, therefore we have decided to exclude the first 15 snapshots of the simulations from the results produced on each subhalo.

3.1 Orbital AM

As a first result we have plotted the evolution of the orbital angular momentum of each subhalo in the five runs, given in Fig. 3.1. Side by side we have plotted the orbital AM as a function of redshift (from redshift $z \sim 6$ to $z = 0$). All AM are expressed in physical units $kpc\cdot\frac{km}{s}$.
We notice that for each subhalo, we observe that there is a clear difference in orbital AM magnitude between each simulation. Indeed, the relative difference with the reference remains positive for $AM_{fid}\times2.0$ and $AM_{fid}\times1.2$, with the former always larger than the latter and remains negative for $AM_{fid}\times0.5$ and $AM_{fid}\times1.05$, with the former always larger than the latter, through all redshifts. This shows that the orbital angular momentum is highly dependent on the initial conditions of the simulation runs, and that the effects of it are felt throughout the entire evolution of the subhalo. In other words, we notice that, there exists an order between the simulations which is consistent between subhalos. No matter the redshift, in increasing order we have $AM_{fid}\times\{0.5,1.05,1.1,1.2,2.0\}$. This reflects the AM settings of the initial conditions where we have explicitly set the AM at the beginning to be such. It is particularly interesting to

see that this order does not change throughout the entire evolution of the subhalos, as this implies that the role of the initial AM is very significant in determining the rest of the evolution.
Furthermore, we have observed that in all subhalos, $AM_{fid}\times 0.5$ evolves with a higher gradient at the high redshifts compared to the others, and its gradients decreases to converge closer to those of the other simulations. Its rate of orbital AM evolution therefore approaches that of the others. For example, in subhalo 3 at redshift $z\sim 6$ the difference in gradient between $AM_{fid}\times 0.5$ and the reference is quite significant, however, at redshift $z = 0$ it has converged towards close to 0%, where we have curves that are parallel in the relative difference plot. Since its orbital AM is lower than those of the others, this change in the gradient is reflected in the other plots. As the AM in $AM_{fid}\times 0.5$ increases at a higher rate and closes the gap with the others at high redshifts, and approaches the other curves asymptotically, such that they become almost parallel at low redshifts.
A similar trend can be observed in the other runs where we have their AM magnitude which converges closer together. This can be seen in the relative difference plot in which we observe that at high redshifts the difference between simulation runs are higher than at low redshift. For example, in subhalo 1, we have that $AM_{fid}\times 2.0$ differs by around 50% at $z\sim 6$, however this changes closer to around 30% at $z = 0$. However, when looking at the evolution of the gradient in redshift (noting the area of higher slopes in the plots), we observe that these changes in AM magnitude occur mostly at specific redshifts (notably redshift $z\sim 1.75$ and $z\sim 1$ to $z = 0$ in subhalo 1). The phenomena acting on these AM momentum changes may therefore be different. This could be due to effects of large major mergers (LMM) of the main halo which propagate onto the satellites.
Interesting to notice is the gradient increase experienced by subhalo 2 at around $z\sim 1$, which is not experienced by the other two. As we shall discuss later, this is due to the way the main halo center was defined, and how this can be disturbed when it undergoes major mergers. In this case, the trajectory of the subhalo was such that the orbital angular momentum was given a "kick".
Going back to $AM_{fid}\times 0.5$ for each subhalo, we find that when we compare it to $AM_{fid}\times 2.0$, there is a clear difference in the relative difference of it's magnitude compared to the reference. Indeed, we have that the former sits around -0.5 to -1.0, while the latter sits around $+0.3$ and $+0.5$. Given that both of these simulations are borne from a change in the initial AM condition to the fiducial simulation which involves dividing by two and multiplying by two, respectively, the relationship that is presented to us is not linear. There is therefore an asymmetry in the effect of changing the AM has on the orbital angular momentum, where reducing the AM has a stronger effect than increasing it.
Overall, we therefore have consistent results between all three subhalos and all five simulation runs indicating that higher initial AM momentum modification leads to higher specific orbital momentum magnitude in the subhalos throughout the duration of the enitre evolution. This result shows that modifying the AM at the early universe persists into low redshifts and has long-lasting effects. The higher initial AM provides the rotational support for central halo which directly increases the orbital angular momentum magnitude of the subhalo.

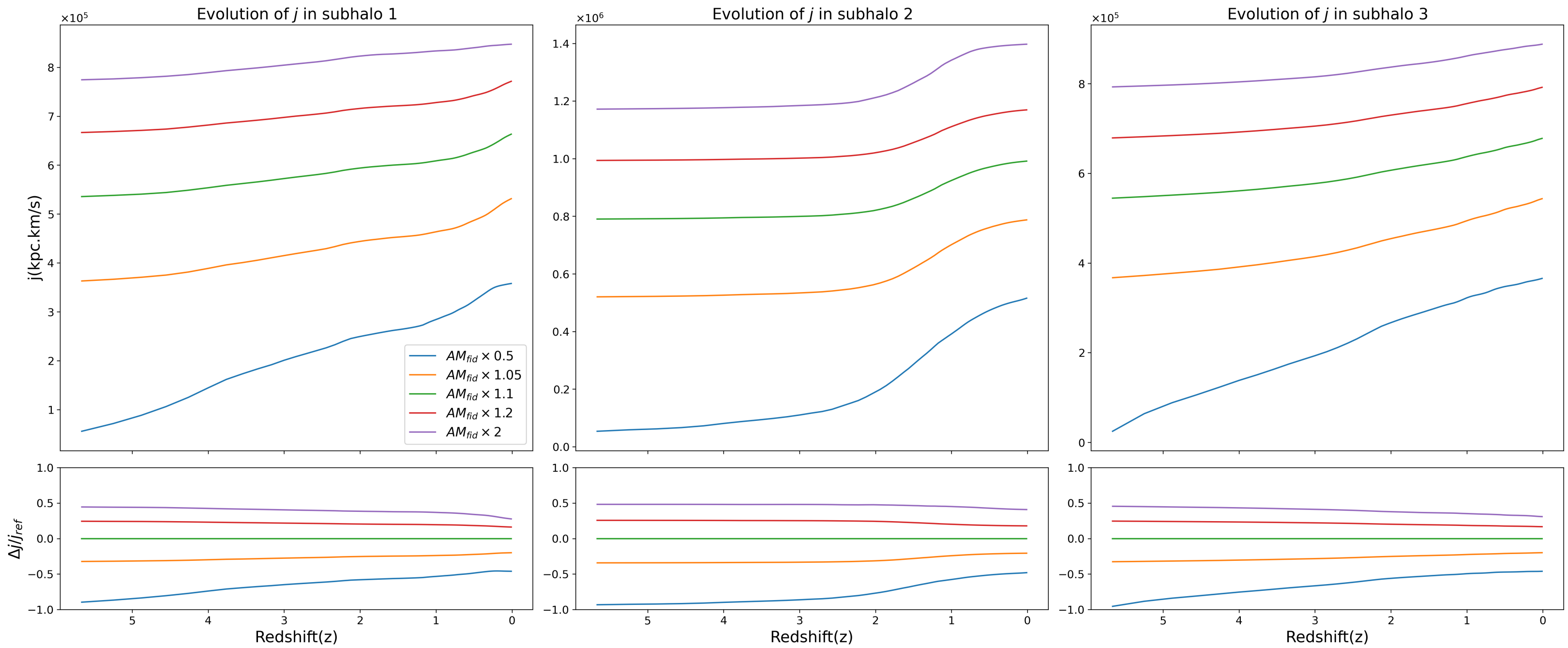

Figure 3.1: Orbital AM Magnitude of the 3 subhalo candidates in 5 different simulation scenarios. Each plot shows one of the subhalo candidates. Each curve refers to the simulation scenario: $AM_{fid}\times0.5$ (blue), $AM_{fid}\times1.05$ (orange), $AM_{fid}\times1.1$ (green), $AM_{fid}\times1.2$ (red), $AM_{fid}\times2.0$ (purple). Top panels show $\mid j \mid$ in physical units; bottom panels show the relative difference with respect to $AM_{fid}\times1.1$. The curves are monotonically ordered by the initial AM condition of the host halo across all 3 subhalos, suggesting the specific orbital AM of subhalos is set by and traces the host halo's AM condition. Furthermore, the asymmetry in the effect the initial AM of the host halo has on the orbital AM properties can be seen in the relative difference plots where we see that $AM_{fid}\times0.5$ deviates much more from the reference than $AM_{fid}\times2.0$ in each subhalo.

3.2 Virial Radius

We present our findings for the evolution of the virial radius in each of the simulations for the different subhalos. This is presented in Fig. 3.2. Side by side we have plotted the virial radius as a function of redshift (from redshift $z \sim 6$ to $z = 0$). All distances are expressed in physical units *kpc*, obtained by converting from commoving coordinates via $r_{kpc} = r_{\mathrm{kpccm}} \cdot a$, where $a = \frac{1}{1+z}$ is the cosmic scale factor. Unlike comoving coordinates, physical proper distance in *kpc* includes the effects of cosmic expansion, representing the true physical separation between objects at a given redshift.

As a first general observation, in each subhalo the virial radius increases monotonically as it evolves in time and approaches $z = 0$. For example, subhalo 1 simulation run $AM_{fid} \times 2$ has virial radius $R_{vir} \approx 5$kpc at $z \sim 5$ and grows to have a virial radius $R_{vir} \approx 20$kpc at $z = 0$. We also have that the different curves in each plot tend to cluster tightly together indicating that the virial radius is largely insensitive to the AM modifications done. Indeed, the deviations from the reference remain between 5-10% at low redshifts. Moreover, as a general trend, in most of the runs the gradient also increases with time.

Let us discuss each subhalo individually, beginning with the first and most massive subhalo. In subhalo 1, for every simulation run, we observe a rather uniform increase in virial radius.

Until $z \sim 1.1$, each run evolves in approximately the same way with the same virial radius (<1% difference). Beyond this redshift, we notice a considerable difference between each run. The gradient of their evolution decreases and in $AM_{fid}\times\{1.05,1.1,1.2,2.0\}$ we notice two dips in virial radii. The first dip occurs around $z \sim 0.9$, and the second occurs at $z \sim 0.8$ for $AM_{fid}\times1.05,1.1,1.2,2.0$. The change in their gradient also differs between the run, with a noticeably smaller decrease for $AM_{fid}\times0.5$ and bigger decrease for $AM_{fid}\times2.0$. This difference in gradient disappears between $AM_{fid}\times0.5,1.05,1.1,1.2$, however persists for $AM_{fid}\times2.0$. This can be seen when looking at the relative difference with the reference, in which we see that at $z \sim 0.5$ the difference is around 10% while at $z = 0$ it is above 20% . As a point of comparison, between $z \sim 0.7$ and $z = 0$, $AM_{fid}\times0.5$ remains roughly at a 5%. A final note is made on the decrease of the virial radius of $AM_{fid}\times0.5$ from redshift $z \sim 0.1$ to $z = 0$. The cause of these differences are dynamical in nature, relating to tidal stripping and will be discussed later.

Subhalo 2 shows a slightly different picture, in which the evolution of the different virial radii for each simulation seems to coincide very closely, even towards low redshift. This correspondence is shown in the relative difference where we see each curve hovering around 0. Their virial radii therefore do not differ largely between simulations. While that is largely the case, we observe a different evolutionary path taken by $AM_{fid}\times2.0$, between redshifts $z \sim 4$ and $z \sim 2.5$ where it's gradient increases slightly leading to a relative difference in virial radius compared to the other runs of around 15%. Moreover, we also notice that at low redshift of this run, the virial radius is slightly lower than that of the others (from redshift $z \sim 1$ down to $z = 0$). $AM_{fid}\times0.5$ also shows a sudden deviation from the others near $z = 0$, similar to what we observed in subhalo 1. The latter divergence is of interest relating once more to tidal stripping and we shall discuss later in chapter 4, however the divergence of $AM_{fid}\times2.0$ at higher redshift is likely due to some dynamical effects which we shall not explore.

This differs slightly from what we see in subhalo 3. Indeed, subhalo 3 shows the same general trend where the virial radii coincide quite well at high redshifts, however at low redshifts ($<z \sim 0.5$) we noticed that both $AM_{fid}\times0.5$ and $AM_{fid}\times2.0$ decreased in relation to the reference, due to a decrease in gradient, diverging from the other three. Furthermore, with subhalo three we observed $z \sim 2$ and $z \sim 0.5$, a

noticeable difference in virial radius for $AM_{fid}\times0.5$ and $AM_{fid}\times2.0$ compared to the others, where the $AM_{fid}\times0.5$ reaches a virial radius around 15% larger than the reference and $AM_{fid}\times2.0$ around 5% smaller. Finally, we also observe a small decline in the gradient of virial radius among all simulations at around $z \sim 1$. The only differences of interest to us are the low redshift divergences that occur.
Compiling the above observations, we notice a few interesting differences and similarities to note. At high redshifts, the virial radii seem to evolve in a similar fashion and at the same values. At lower redshifts however, there are cases of divergence in virial radii between simulations. While subhalos 1 and 3 show that the runs with lower AM in the initial conditions have slightly higher virial radii throughout (excluding occasional bumps and very low redshifts in the case of subhalo 3), subhalo 2 shows the opposite trend until redshift $z \sim 1$. This is likely a random effect occuring at the initialization of the subhalo, and therefore unrelated to the AM of the central halo. Subhalo 1 and 2, at low redshift ($< z \sim 1$) showed a pattern of diverging virial radii between simulations, with lower AM leading to higher virial radius, possibly linking AM initial conditions to low redshift subhalo size. Subhalo 3 corroborates this in part, with $AM_{fid}\times0.5$ posing as an anomaly in this and producing the lowest virial radius subhalo. It is therefore highly unlikely that the initial AM conditions are directly linked to the low redshift subhalo sizes and it is more likely that these are consequences of other dynamical effects such as tidal stripping, which we shall discuss further in 4. The results we observe are therefore due to indirect effects, such as on trajectory, of changing the AM. With this few subhalos to analyse, nothing conclusive can be can be extracted. However, as a whole we observe an insensitivity of the virial radius to the initial AM modification, with certain dynamical effects leading to differences between each runs, which we shall discuss in the following sections.

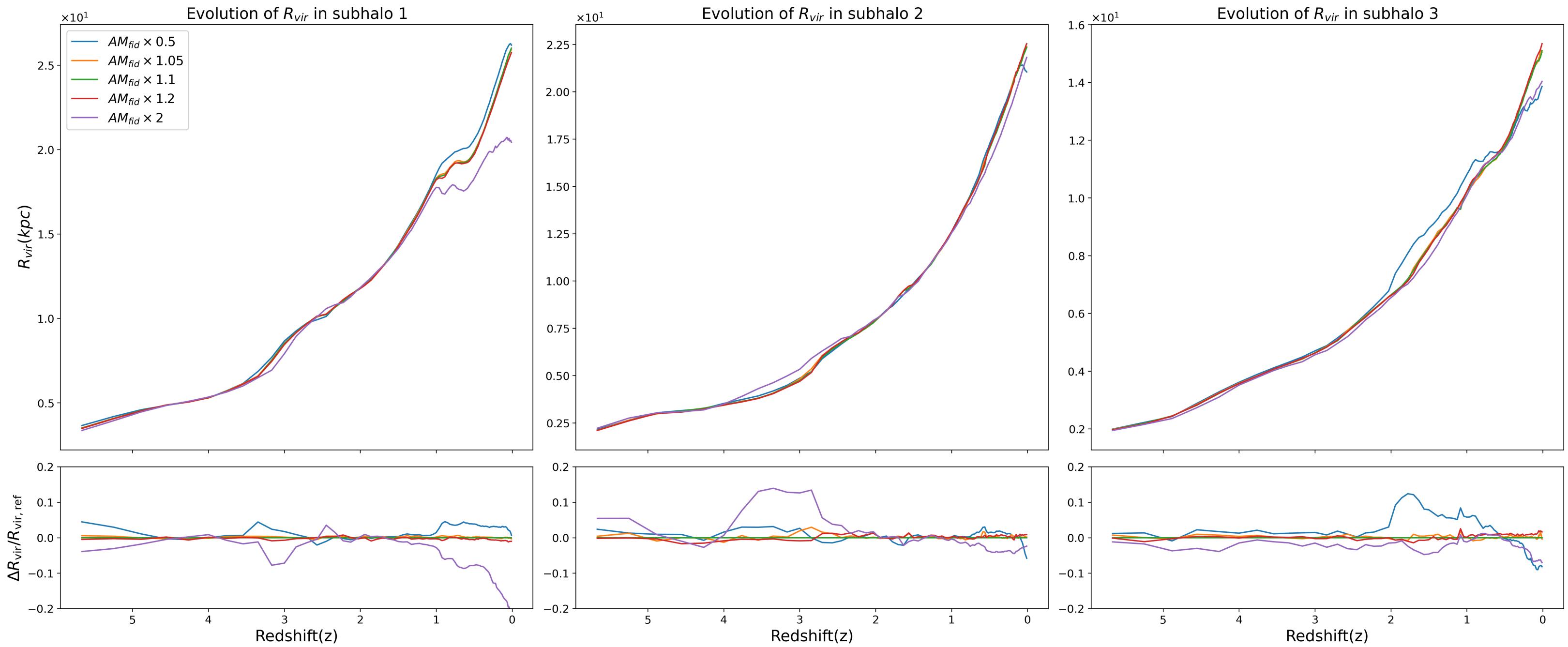

Figure 3.2: Virial Radius of the 3 subhalo candidates in 5 different simulation scenarios. The layout of the plot and curves follows Fig.3.1. Top panels show R_{vir} in physical units; bottom panels show the relative difference with respect to $AM_{fid}\times 1.1$. The curves deviate remain largely consistent with each other at high redshifts ($z \gtrsim 1$) suggesting an insensitivity of a subhalo's virial radius to initial AM modification of the host halo. The deviations at low redshifts are consistent with tidal stripping effects at late times.

3.3 Virial Mass

The evolution of the virial mass of the subhalos is presented in Fig. 3.3. The findings are presented in physical units $M\odot$ for the same reasons mentioned earlier with regard to the use of *kpc* for the virial radius. We have also plotted the relative difference of each virial mass with respect to $AM_{fid}\times1.1$.
We observed similar trends to those discussed for the virial radius in Sect. 3.2. We observe that all simulations therefore broadly follow the same mass growth history, where we have continuous increase at high redshift followed by a peak around $z\sim1-1.5$ and then a decrease or flattening of the curves toward $z\sim0$. Moreover, general trends show the curves tend to cluster together which indicates that they are largely insensitive to the initial AM modification. In fact, throughout most of the evolution, the relative difference between any other simulation run and the reference does not deviate by more than around 10% (excluding anomalies such as in $AM\times2.0$ in subhalo 2 around $z\sim3$ which are likely not a consequence of initial AM modification). These results therefore concur with those we observed for the virial radius in Sect. 3.2.
This is to be expected due to the relation linking radius (R) to mass (M) in a sphere: $M=\bar{\rho}(z)\frac{4}{3}\pi R^3$ where $\bar{\rho}(z)$ is the average density in the spherical volume.
While we observe these general trends, it is worth noting that there are behaviours that are worth pointing out and that may indicate that effects other than the initial AM modification might be intervening.
It can be seen that in subhalos 1 and 3 the higher initial AM condition runs produce subhalos with smaller virial mass until redshift $z\sim1$ for the latter and throughout the entire run in the former. Moreover, we observe the same inverted effect as was observed when investigating the virial radii in subhalo 2 where the higher initial AM condition subhalos have larger virial masses. The same effect is likely the cause in both instances.
Furthermore, when in the virial radii plots we noticed that there are bumps around redshift $z\sim3$ and $z\sim1$ for subhalo 1, and we observe similar noticeable bumps in our virial mass plots. However, while the virial radius continues to grow after the second bump, the viral mass drops considerably in all simulations, going from $1.8\times10^9M\odot$ at its peak to around $1.2\times10^9M\odot$ at its lowest for run $AM_{fid}\times0.5$. We also notice an additional dip in $AM_{fid}\times2.0$ at around $z\sim0.2$.
In subhalo 2, between redshift $z\sim4$ and $z\sim2$, we observe the similar divergent evolution of $AM_{fid}\times2.0$, which ends up around 50% more massive than the reference. It increases steeply and remains relatively more massive than the rest between $z\sim2.8-3.5$, before decreasing and rejoining the ensemble. This divergence likely does not relate to the initial AM modifications made. Between redshift $z\sim1$ to $z\sim0$, we observe a drop in $AM_{fid}\times2.0$ followed by stagnation, while for $AM_{fid}\times0.5$ we observe a stagnation followed by a sudden increase and drop. This differs from the other simulations which stagnate, increase slightly and return back to their stagnation value.
In subhalo 3, we notice that same bump observe in the virial radius plots between $z\sim2$ and $z\sim1$, where we have a large increase in $AM_{fid}\times0.5$'s mass, and lower increases in masses for the other runs. We therefore get that the $AM_{fid}\times0.5$ run diverges from the other simulations at the bump, before returning back around $z\sim1$, when the values for the virial masses drop in all simulations. We then also have that the virial masses for both $AM_{fid}\times0.5$ and $AM_{fid}\times2.0$ drop below those of $AM_{fid}\times1.05$,1.1,1.2 at redshift $z\sim0.5$. The effect at the root is tidal stripping and it will be discussed in the later chapter.
When looking at the virial mass, we observe very similar results to those of the virial radius, with each

subhalo evolving slightly differently due to their unique characteristics, however general trends show that this property is largely insensitive to the effects of initial AM modification. Other dynamical effects, influenced by the change in AM, are likely responsible for the anomalous behaviors we observe in the different subhalos.

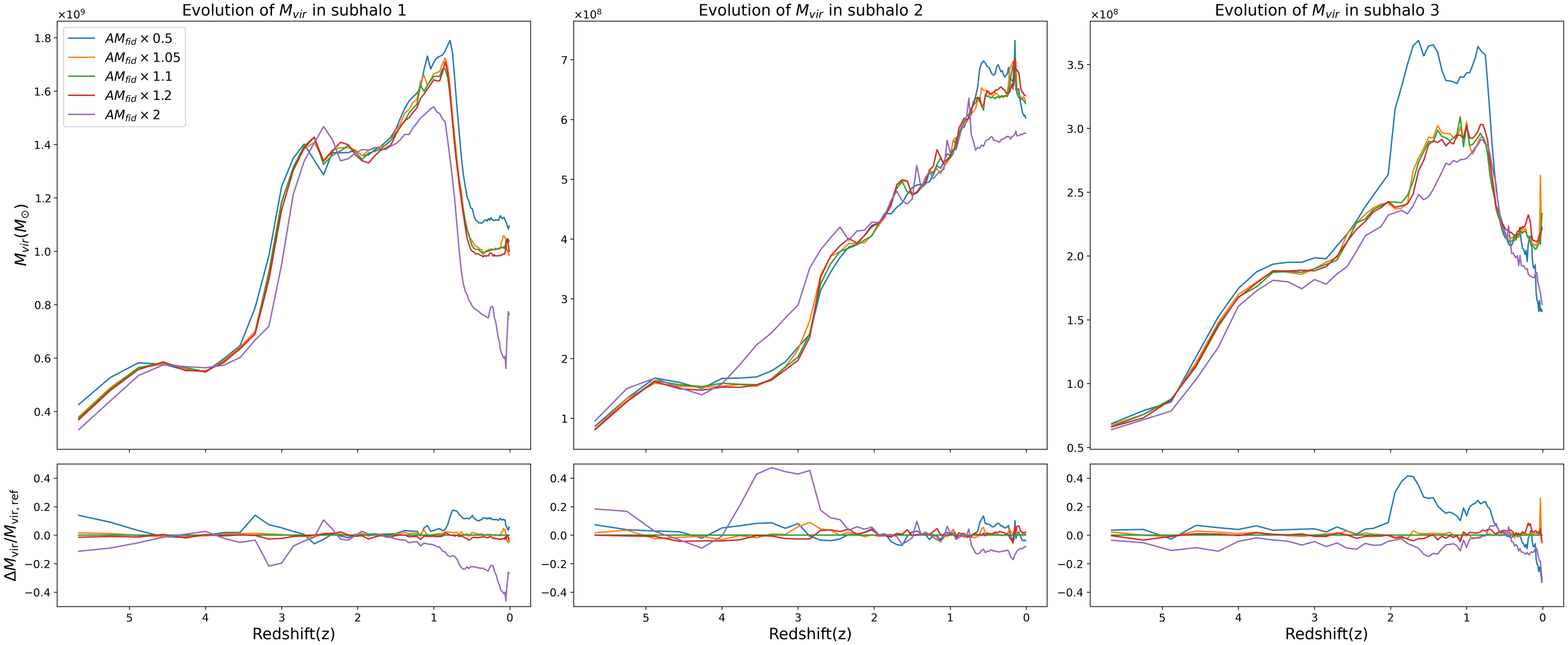

Figure 3.3: Virial Mass of the 3 subhalo candidates in 5 different simulation scenarios. The layout of the plot and curves follows Fig.3.1. Top panels show M_{vir} in physical units; bottom panels show the relative difference with respect to $AM_{fid}{\times}1.1$. As with Fig.3.2, the curves remain largely consistent with each other at high redshifts ($z \gtrsim 1$) suggesting an insensitivity of a subhalo's virial mass to initial AM modification of the host halo, with the deviations at low redshifts likewise consistent with tidal stripping effects.

3.4 Radial Distance to Central Halo

The evolution of the radial distance to central halo of the subhalos is presented in Fig. 3.4. The findings are presented in physical units *kpc* for the same reasons mentioned earlier in the previous subsections. We have also plotted the relative difference of each radial distance with respect to $AM_{fid}\times 1.1$.

At first glance we see that the general trend of all subhalos in these plots is broadly similar, where we have a relatively constant evolution at high redshift followed by a sharp decrease at low redshift corresponding to the subhalo falling toward the central halo.

As we have done previously, let us discuss subhalo 1. We first observe that at high redshift, between $z\sim 6$ and $z\sim 1$, their is a correlation between radial distance and initial AM magnitude, where the simulation runs with small initial AM magnitude have larger radial orbits and vice versa. For example, at redshift $z\sim 2$, $AM_{fid}\times 0.5$ has a radial distance around $3\times 10^2 kpc$, $AM_{fid}\times 1.05$,1.1,1.2 have radial distances of around $2.5\times 10^2 kpc$ (with slight differences between the three such that they respect the observation that lower AM correlate to higher radial distance) and $AM_{fid}\times 2.0$ has a radial distance just below $2.5\times 10^2 kpc$. There is nothing to suggest that we have causation however, and we observe the opposite effect in subhalo 2. Moreover, we noticed that the gradient between the simulation scenarios evolve differently between that same interval. Indeed, the lower AM initial conditions tend to show a higher gradient, thereby moving further away from central before its initial fall in towards the central halo around $z\sim 1.75$. It is interesting to note that there is an initial collective drop in radial distance around $z\sim 2$ of around $0.25\times 10^2 kpc$. This is caused by issues in computing the center of the main halo when it is undergoing a major merger and is purely numerical and not an effect of a physical nature.

During the first inspiral occurs at slightly different redshifts depending on the initial conditions - taking place earlier for subhalos closer to the central galaxy. They travel around $2kpc$ inside before traveling out. The outspiral similarly occurs earlier. A second inspiral occurs at around $z\sim 0.5$ for $AM_{fid}\times 0.5$,1.05,1.1,1.2, with a slight bump occuring at around $z\sim 0.7$. This is also an effect related to the main halo center computation. Interesting to note is that $AM_{fid}\times 2.0$ has two inspirals during the same interval of time, with one occuring around $z\sim 0.75$ and another occuring around $z\sim 0.2$.

A different picture emerges in subhalo 2, where we have that the simulations with higher initial AM conditions have larger radial orbits a high redshifts and up until $z\sim 0.25$. For example,at its peak difference at $z\sim 1$, we have $AM_{fid}\times 0.5$ at around $5\times 10^2 kpc$ and $AM_{fid}\times 2.0$ at around $7\times 10^2 kpc$ $AM_{fid}\times 2.0$. Thus, throughout the evolution, we observed the opposite pattern to that of subhalo 1. Moreover, we observe the same differences regarding the evolution of the gradient among the different simulations with inverted order (ie. higher initial AM condition simulations gradients increasing more rapidly in the first stage of the evolution - up until $z\sim 1$). This gives strong arguments to suggest that the diverging of the radial distance is merely an effect of the initial radial distance and not anything inherent in the conditions laid out by the AM.

The inspiral in subhalo 2 occurs around redshift $z\sim 1$, each simulation run following a similar infall curve. Interesting to note is that the inspiral occurred faster for $AM_{fid}\times 2.0$, leading to a steeper negative gradient as well. We also notice a slight increase in radial distance at very low redshift (close to $z\sim 0$) of $AM_{fid}\times 0.5$, which indicates that $AM_{fid}\times 0.5$ could be going through the different stages of evolution of the subhalo quicker than the others.

We now look towards subhalo 3, and observe similar trends to subhalo 1, where at high redshifts we see that the lower initial AM conditions have higher radial orbits. However, unlike subhalo 1 we have a rather different behaviour when looking at the gradient of the evolution. While in subhalo 1 we observe gradients that diverge towards lower redshifts, in subhalo 3 we observe gradients that remain quite constant between simulations until redshift $z \sim 2$. We then have a convergence of the radial distances in which $AM_{fid}\times2.0$ increases and $AM_{fid}\times0.5$ decreases. At $z \sim 2$, the subhalos in all five runs have a radial distance of around $2.25 \times 10^2 kpc$.

After the convergence of radial distances, the paths of the curves become somewhat messy. The lower inital AM subhalos experienced the inspiral first, as was the case in subhalo 2. Moreover, $AM_{fid}\times0.5$ experiences the shortest outspiral from the center followed by $AM_{fid}\times2.0$, peaking around $2.25 \times 10^2 kpc$ and $2.5 \times 10^2 kpc$ respectively. $AM_{fid}\times1.05,1.1,1.2$ all peak at around $3 \times 10^2 kpc$.

A second inspiral and outspiral occurred for both $AM_{fid}\times0.5$ and $AM_{fid}\times2.0$. For the former, the outpiral reached its peak, while the latter showed an increasing trend at $z = 0$. For $AM_{fid}\times1.05,1.1,1.2$ we observed an inspiral which reached their local minimum radial distance from the central halo, and showed the beginnings of an upwards trend at $z \sim 0$. We notice in these three that, as was the case in subhalo 2, the higher initial AM subhalos have the higher radial distance. These numerous inspirals and outspirals are characterstic of more eccentric orbits around the central halo.

Subhalo 3 seems to show both the characteristics of subhalo 1 and subhalo 2. In the first half it follows a similar evolution portrayed by subhalo 1, but during the convergence of radial distances that occurs at $z \approx 2$, the correspondence shifts, and the subhalo embodies similar characteristics to subhalo 2. What we see are very different evolutionary paths that subhalos can take, the impact of which is not only dictated by the initial AM condition but of other factors such as the initial radial distance of the subhalo.

An effect that should be considered are the major mergers within the central halo. Indeed, these mergers between DM halos that are similar in mass produce very strong gravitational fields and unorthodox density distributions. For example, one of these can be observed around the redshift $z \sim 1$. This leads to a much more difficult determination of the center of mass of the main halo. This center therefore "shifts", and the subhalos move relative to this dynamical center. These features appear in the radial distance plots where we observe in Fig. 3.4 at redshift $z \sim 1$ for subhalo 2, a small bump. Indeed, we see that the radial distance increases slightly before decreasing. This is therefore simply an artifact of not properly locating the center of the main halo. This could be circumvented in future by defining the center as the median of a small subset of the most tightly bound particles in the main halo. In this case, one would take the median as certain particles may still be ejected out, and this would act to preserve the proper center in such circumstances. Moreover, notice that the timing at which this bump appears is slightly different between the simulation runs, this is an effect of changing the initial AM, which induces a change in the timing of the major mergers.

An overview of our results show that all subhalos broadly undergo similar evolution and that the differences between these are likely due to dynamical effects with strong dependence on orbit trajectory. These radial distance plots will allow us to put the evolution of the other properties into context and interpret our results. This will be discussed further in the following section.

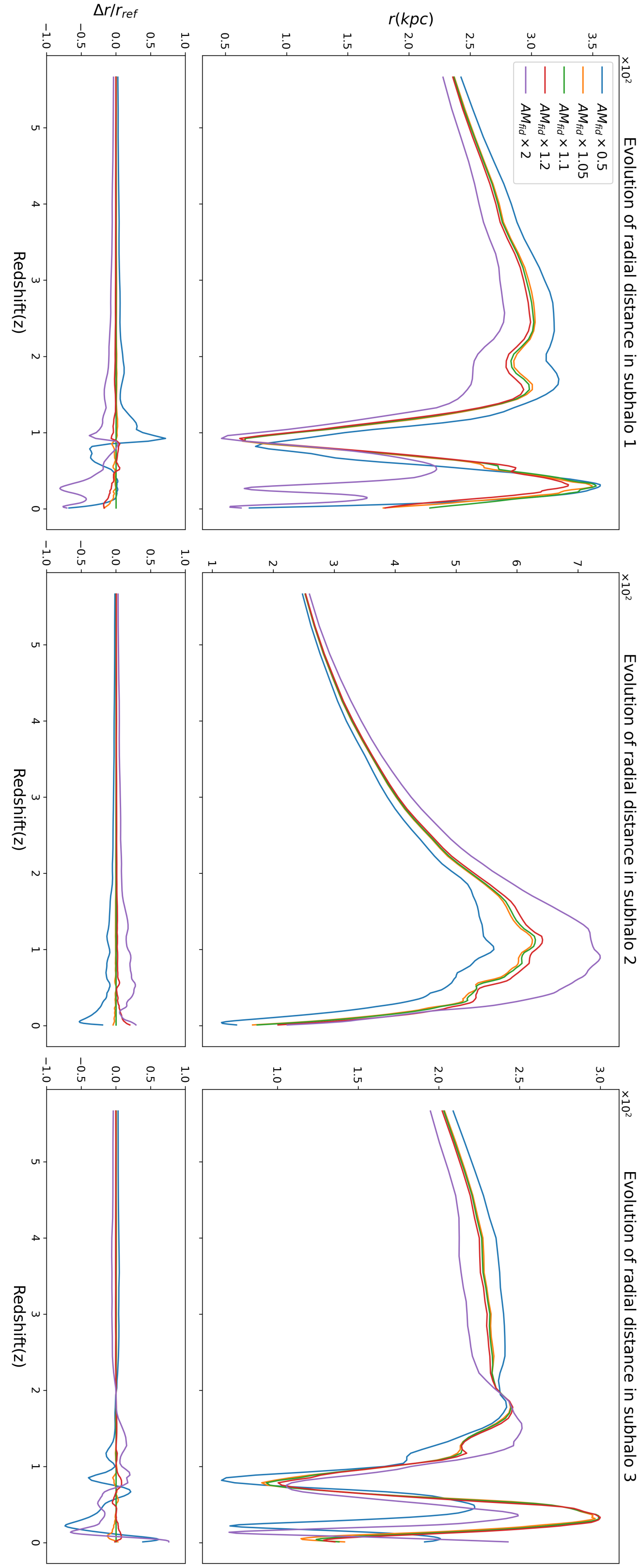

Figure 3.4: Radial Distance from the Central Halo of the 3 subhalo candidates in 5 different simulation scenarios. The layout of the plot and curves follows Fig.3.1. Top panels show the radial distance r to the central halo in physical units; bottom panels show the relative difference with respect to $AM_{fid}\times1.1$. The plots show the infall and pericentric passages of each subhalo at low redshift ($z \lesssim 2$). Unlike the specific AM, the radial trajectories show no clear monotonic ordering with respect to the host halo's initial AM, suggesting the trajectories are less sensitive to the host's initial AM condition.

In summary, the results presented in this chapter provide a clear and physically consistent picture that directly addresses the central aim of this thesis. While the initial AM of the central halo leaves a persistent and ordered imprint on the specific orbital AM of the satellite subhalos, it has little direct impact on their virial radius and mass. The low-redshift deviations observed in these structural properties are instead linked to differences in orbital trajectories and the associated tidal stripping, both of which are indirectly influenced by the initial AM modification. These results are discussed and placed in the context of today's literature in Chapter 4.

Chapter 4

Discussion, Caveats and Conclusions

In this chapter we discuss and interpret the results obtained in Chapter 3, placing them in the context of the existing literature on the relevant physical phenomena (Sect. 4.1). We then discuss the limitations of our work and the caveats that should be considered when interpreting our results (Sect. 4.2). Finally, we summarise the key findings of this project in relation to the central research question and outline directions for future work (Sect. 4.3).

4.1 Discussion

Let us first discuss the most robust result in this work which relates to the consistent ordering of the specific orbital angular momentum magnitude across all five simulations and in all three subhalos. In Sect. 3.1, we have shown that the specific orbital angular momentum is highly sensitive to the initial AM conditions, and that in all cases, higher initial AM in the central leads to higher orbital AM in the subhalos. This result is consistent with what is expected in a gravitationally dominated environment such as this, where we do not have the presence of other processes in the system that could perturb its evolution. We can connect this observation to TTT and find that this is consistent with the theory. Indeed, TTT predicts that the AM of structures at low redshifts is determined by the tidal fields generated by large scale structures in the early universe. As discussed in the Sect. 2.4, when we modify the AM of the central halo, we are effectively modifying the initial density distribution of the universe and hence the tidal field in which the subhalos evolve. During the condensation period of the halos, the central halo acquires AM, and the subhalos that form similarly acquire their orbital AM. Throughout the evolution, the ordering set by the AM initial conditions is preserved, which suggests that the initial AM leaves a lasting imprint on the orbital structure of subhalos and that subsequent dynamical evolution does not erase this. However, it is worth considering how the method used to select the subhalos, described in Sect. 2.4, may influence these results. The observed ordering of the specific orbital angular momentum across all five simulations in all three subhalos are consistent with today's literature. Indeed, Cadiou et al. (2021) found, using a suite of genetically modified cosmological simulations analogous to this work, that the AM of the DM lagrangian patch evolves proportionally to its initial value. A relation is obtained to get the AM of the modified simulation as a function of its value in the fiducial. This is given in the following formula they have derived:

$$l_{pred}(z) = l_0 \times \frac{l_{ref}(z)}{l_{ref,0}}$$

$l_{pred}(z)$ is the predicted AM in the lagrangian patch and therefore the central halo, and l_0 is its initial value. l_{ref} is the AM in the fiducial simulation and $l_{ref,0}$ its initial value. The angular momentum therefore evolves non-chaotically, determined by the environment and is an intrinsic property of a given region. The above formula therefore implies that in a gravitationally dominated system, in which no dissipative forces are present to redistribute the AM, the ordering established in the initial conditions is preserved throughout the duration of the cosmic evolution. Due to the absence of baryonic matter, DMO simulations are indeed gravitationally dominated. While the relation derived by Cadiou et al. (2021) strictly applies to the internal AM of the central halo's lagrangian patch region, rather than the orbital AM of subhalos, the underlying physical argument remain applicable. Notably, the effects of the modifications extend to 60Mpc/h. Since the system is governed solely by gravity, the ordering imposed by the initial conditions imprints onto the orbital properties of the subhalos.

Let us now focus our attention on the results that show very little correlation between initial AM condition. We have observed in Sect. 3.3 and Sect. 3.2 that in our results, both subhalo virial mass and virial radius show an insensitivity to the initial AM condition, and evolve very similarly throughout the simulation duration. This can be seen in Fig. 3.2 where we see that in most cases, each run deviates less than 10% from the reference. These observations display that the virial mass and virial radius have a higher dependence on the accretion history and less on the initial AM condition. While we see little dependency, there exists differences in the evolution of these properties. In particular, these differences are observed most prominently in low redshifts. This indicates that the physical phenomena involved causing these difference strictly occur at late times. We know that as the subhalo evolves, it is brought closer to the central halo. Indeed, this can be seen in Sect. 3.4, where the radial distance can be seen to drop at lower redshifts. An effect that is observed as subhalos are brought closer to the center and therefore to higher density regions is tidal stripping. Tidal stripping involves the process by which a subhalo loses mass in its outer regions due to the competing tidal forces of the host halo and the self-gravity subhalo. As the subhalo approaches the host halo, the latter's gravitational potential increases and eventually exceeds the binding energy of the subhalo particles in the outer layers. Thus, since this is a gravitational effect, it is highly dependent on the subhalos orbit. In each run the subhalo approaches the central halo with a different trajectory, and therefore is tidally stripped in a different manner. This results in slightly different curves between runs at lower redshift. We thus have that the AM and the initial gravitational forces determine the trajectory of the subhalo, which then determines the tidal fields it later experiences, and these tidal fields determine how much mass is tidally stripped.

In this way we are able to reconcile the virial radius and mass plots with the radial distance plot, in order to get a more complete picture. When cross referencing the three plots and their timings we notice that the mass loss and therefore the virial radius decline occur roughly during the peri-centric passage of the subhalo around the main halo. We define the peri-center to be the point of minimal radial distance of a subhalo to the central halo. Similarly, we define the apocenter for a subhalo to be the point of maximal distance from the central halo. This is visible in subhalo 1 at redshift $z \sim 1$ where we have the first peri-centric passage for the different simulation runs. At the peri-center and the out-spiral, we notice the occurrence of the most mass loss and virial radius decline. Indeed, these phenomena seem to coincide. This is consistent with the literature out there today regarding the timing of maximal mass loss for a subhalo trajectory. It was found by Diemer et al. (2024), in the halo samples they analyzed that half of subhalo losses occur around the peri-center (which they define as within 30% of the smallest distance they record). This is due to the high gravitational potential near the center, which leads to increased tidal forces. However, they note that while a large portion of the mass loss occurs during at and around the peri-center, this mass loss can continue further into the outspiral and into the apo-centric passage. Counterintuitively, the mass loss may therefore not occur entirely during the times when the tidal forces are strongest. This picture corroborates what we observe in our results, which indicate a correlation between mass loss and orbital trajectory close to the central halo and the subsequent outspiral.

The dynamical effects explained above are largely responsible for many of the features described in our observations. Our results suggest that the dominant driver in mass loss of subhalos is therefore tidal stripping, the severity and timing of which is determined by the orbital trajectory of the subhalo.

For example, this explains the divergence that occurs around $z \sim 1$ and z=0 in subhalo 1 of the virial radius plot. Indeed, cross comparing with virial mass plot and the radial distance plot, we are able to link the trajectory to the mass loss. This pattern is suggestive of tidal stripping occurrence. Moreover, this analysis elucidates the dip in the virial radius for $AM \times 0.5$ in subhalo 2. Indeed, at that point in its evolution, it is at the peri-center and outspiraling, which leads to mass loss that translates into a decrease in the virial radius. In this way, many of our observations are consistent with today's literature on the subject, and we have managed to determine the sensitivity and dependency of certain subhalo properties to the initial AM of the main halo. However, we are limited by several aspects of our project which needs to be considered when interpreting our results.

4.2 Caveats

It is important to consider the context around our results and define the limitations that are present.

To be considered first are the statistical limitations involved in having a dataset of 3 subhalos. This very limited sample size leads to very few results that can be statistically generalized, and a large variance can be observed in our results. In order to get a more statistically significant results, we would need a larger sample size of subhalos as it could be that the results we have are specific to the specific merger history and environment of the selected subhalos. Furthermore, it is worth mentioning that the subhalos were all selected from one host halo, and in order to properly generalize the results, one could analyze and compare between observations made of subhalos from different halos.

A second limitation to be considered is the method we used to find the subhalos. Indeed, the method we used involves particle identification between snapshots, as well as particle identification between simulation runs at low redshift. This comparison between particle IDs biases the subhalos that are found to those that have more particles in common. Mergers between subhalos and those that undergo collisions are therfore unlikely to be found, and therefore are not present in our subhalo candidates. Indeed, none of the subhalos we have selected undergo a collision or merger during its evolution. While we are not particularly interested in these dynamical phenomena, it is important to mention how our results do not reflect their presence. Indeed, the method considered tracks particle IDs and implements a matching algorithm of the most central particles in the subhalo at early redshift in order to retrieve the subhalo at earlier snapshots. Moreover, in order to find the same subhalo in each run of the simulation, we used a particle ID matching process which will tend to bias subhalos that have not undergone any large mergers as this leads to a scattering and mixing of particles. The subhalo dataset we are therefore analyzing may be biased towards subhalos that do not experience large mergers during their evolution and therefore have a restricted dynamical evolution. All dynamical phenomena may not be considered, which requires further analysis to be done on all subhalos with vastly different dynamical evolutions.

Furthermore, at low redshift, as the subhalos are more acutely tidally stripped, this method becomes slightly less reliable to match particles between simulations.

A further limitation concerns the numerical resolution of the simulations. Tidal stripping operates most efficiently on the outer, loosely bound particles of the subhalo, which implies that one needs sufficient particle resolution in the subhalo outskirts in order to accurately resolve this process. At low redshift, when the subhalos have lost a significant portion of their mass, it may be insufficient to reliably track their subhalo properties with the number of particles that are available. Indeed, Diemer et al. (2024) found that halo finders such as ROCKSTAR can lose track of heavily stripped subhalos despite a large number of particles still describing them. They thus find that the measured properties of subhalos at low redshift may therefore be affected by numerical effects rather than physical effects.

Another aspect to consider is the use of a single set of initial conditions to derive these results - the only modification involving the AM of the main halo. While this is ideal in order to ensure controlled comparison, it also leads to results that are derived from a particular large-scale environment and merger history. In order to determine fully whether the trends that we observe in our results are true in all environments, a statistical ensemble of simulations would be required, each with a different set of initial conidtions - beyond AM modification.

A final limitation is present in the conditions set by the simulation. We are analysing data from a DMO simulation, which allows us to isolate dynamical effects that change when modifying the AM. In this way we are able to reduce degeneracies and remove the effects of baryonic processes from the equation, which may lead to more ambiguous results. However, this also provides a model which does not give the full picture, and we are not able to see all the different processes at play, and how they may influence the formation and evolution of the central halo and the subhalos.

For example, Gnedin et al. (2004) found that the inclusion of gas cooling in simulations, a baryonic effect, led to increased subhalos densities and steepness in the radial profile in the inner regions. Indeed, as the gas cools, baryon sink to the center and we get adiabatic constraction of DM. According to Weinberg et al. (2008), this added density provides a higher resistance to tidal disruption. In this way the dynamics and observations in the inspiral would be heavily modified with the inclusion of baryonic content.

On the other hand, including other baryonic effects such as supernova and AGN feedback can have the opposite effect. Zolotov et al. (2012) found that in massive satellite projenitors ($M_{vir} > 10^7 M_\odot$ and stellar mass $M_* > 10^9 M_\odot$) the supernova feedback described in their model that occurs from the star formation before inspiral leads to reduced DM densities and shallower inner density profiles. This makes them more susceptible to tidal stripping during inspirals. The inclusion of AGN also influences the density profile with Peirani et al. (2017) having performed a cross comparison between three suites of large cosmological hydrodynamical simulations (Horizon-AGN,Horizon-noAGN and Horizon-DM), and suggesting that this would result in the flattening of the halo density profiles.

While it can be useful to neglect the baryonic effects in order to study the purely dynamical components of a halos development, they cannot be ignored when modeling a complete picture of galaxies and DM halo evolutions.

4.3 Conclusion and Outlook

In this work we investigated the influence of the initial angular momentum of a central dark matter halo on the orbital and structural properties of its subhalos, using a suite of five cosmological zoom-in DMO simulations in which the initial AM was varied by factors ranging from 0.50 to 2 relative to a fiducial value. Three subhalos were tracked across all five simulations from $z \sim 6$ to $z = 0$, and their specific orbital angular momentum $|j|$, virial mass M_{vir}, virial radius R_{vir}, and galactocentric radius were measured and compared across runs.

The key findings of this work are as follows. In our analysis we found that there is a strong correlation between the central halos initial AM condition and its subhalos specific orbital AM evolution. The latter evolves monotonically and conserves the order set by the initial AM condition. While we were able to find a direct link between the above properties, we found that the virial radius and mass of the subhalos were largely insensitive to the changes of initial AM throughout most of the analyzed redshift range. At lower redshifts, we observed significant deviations between the different simulation runs, consistent with tidal stripping on close orbits.

Taken together, these results demonstrate that the initial AM of the central halos leave lasting imprints on the orbital properties of subhalos, notably the specific orbital AM and thus its trajectory. However, the main parameters by which we define them such as virial radius and virial mass remain independent - with the caveat that the trajectory may be modified and lead to differences at low redshifts.

Moreover in the process of obtaining these results we developed a method for identifying subhalos and tracking them throughout the course of their evolution. This involved identifying the inner most particles in the subhalos and using their particle IDs to get the subhalos' mean positions (unbound particles were systematically removed through σ-clipping). An algorithm involving the comparison of position and virial radius was then used to match the correct `ROCKSTAR` subhalo to the particles. Finally, to ensure that the same subhalo was present in all runs of the simulations, a particle ID cross comparison was done at the final snapshot. This method provides a way in which to identify subhalos that have not undergone major collisions, leading to significant particle mixing and escaping.

To summarize our findings and respond to the thesis question, we found the following

- The specific orbital AM of the satellite subhalos is strongly and persistently sensitive to the initial AM condition: the ordering is set by the initial conditions and is preserved throughout their evolution without exception from $z \sim 6$ to $z = 0$ across all three subhalos.
- The virial radius and virial mass are largely insensitive to the initial AM modification, deviating by less than 10% from the reference run (which we took to be the simulation with initial angular momentum $AM_{fid} \times 1.1$) across most of the redshift range.
- At low redshift, both quantities show deviations between runs that are consistent with tidal stripping, whose severity and timing are indirectly set by the initial AM through its effect on the orbital trajectory.

- The radial distance results are physically consistent with the orbital AM results and produce results that help explain the orbital and structural properties into a coherent picture.
- A method for identifying, matching and tracking subhalos across snapshots and simulation runs was developed, effective for subhalos having undergone minimal particle disruption (notably via collisions)
- The effect of AM modification on the orbital AM appears asymmetric; reducing the initial AM condition has a stronger effect than increasing it

This work primarily investigated the properties discussed above and provides a method for identifying the same subhalos in a suite of simulations with genetically modified initial conditions. It leaves room for several future extensions.
Most directly, the inclusion of baryonic physics would allow for a cross-comparison between baryonic simulations and DMO-simulations, providing a more complete picture of the physical processes involved in subhalo evolution and better constraining the effects of changing the initial AM condition on subhalos. Furthermore, the analysis could be extended to a larger sample of subhalos across multiple host halo evolutions. This would provide us with more statistically significant results, as well as give a more general picture of the effects of modifying the initial AM of the main halo on the subhalos.
The robustness of these results could also be tested by performing a cross-comparison between simulation codes, such as AGORA. By comparing codes, the artefacts specific to numerical implementation can be identified and ignored. Additionally, one can also compare with the HARKONENS suite of simulations. Finally, given the strong correlation we found between the host AM and subhalo orbital AM, it would be especially interesting to look at the spin alignment and spin parameters of the subhalos and their evolution. These are internal properties of DM halos, that may give insights to how larger main halos affect the dynamics of their subhalos.

List of Abbreviations

AGN Active Galactic Nuclei

AM Angular Momentum

AMR Adaptive Mesh Refinement

CDM Cold Dar Matter

DM Dark Matter

DMO Dark Matter Only

FOF Friends-of-Friends

GM Genetic Modification

HDM Hot Dark Matter

MPI Message Passing Interface

MW Milky Way

SO Spherical Over-density

SPH Smoothed Particle Hydrodynamics

TTT Tidal Torque Theory

WDM Warm Dark Matter

ΛCDM Lambda Cold Dark Matter

Bibliography

Aghanim N., et al., 2020, Astronomy & Astrophysics, 641, A6

Behroozi P. S., Wechsler R. H., Wu H.-Y., 2013, ApJ, 762, 109

Binney J., Tremaine S., 2008, Galactic Dynamics: Second Edition

Biviano A., 2000, From Messier to Abell: 200 years of science with galaxy clusters (arXiv:astro-ph/0010409), https://arxiv.org/abs/astro-ph/0010409

Blumenthal G. R., Faber S. M., Primack J. R., Rees M. J., 1984, Nature, 311, 517

Book L. G., Brooks A., Peter A. H. G., Benson A. J., Governato F., 2011, Monthly Notices of the Royal Astronomical Society, 411, 1963

Boylan-Kolchin M., Ma C.-P., Quataert E., 2008, Monthly Notices of the Royal Astronomical Society, 383, 93–101

Bullock J. S., Kolatt T. S., Sigad Y., Somerville R. S., Kravtsov A. V., Klypin A. A., Primack J. R., Dekel A., 2001, Monthly Notices of the Royal Astronomical Society, 321, 559–575

Cadiou C., Pontzen A., Peiris H. V., 2021, Monthly Notices of the Royal Astronomical Society, 502, 5480–5486

Codis S., Pichon C., Pogosyan D., 2015, MNRAS, 452, 3369

Dalcín L., Paz R., Storti M., 2005, Journal of Parallel and Distributed Computing, 65, 1108

Davis M., Efstathiou G., Frenk C., White S., 1985, The Astrophysical Journal, 292

Diemer B., Behroozi P., Mansfield P., 2024, Monthly Notices of the Royal Astronomical Society, 533, 3811

Doroshkevich A. G., 1970, Astrophysics, 6, 320

Fall S. M., Efstathiou G., 1980, MNRAS, 193, 189

Frenk C. S., et al., 1999, The Astrophysical Journal, 525, 554–582

Gnedin O. Y., Kravtsov A. V., Klypin A. A., Nagai D., 2004, ApJ, 616, 16

Goldbaum N. J., ZuHone J. A., Turk M. J., Kowalik K., Rosen A. L., 2018, Journal of Open Source Software, 3, 809

Gunn J. E., 1977, ApJ, 218, 592

Hoffman Y., Ribak E., 1991, ApJ, 380, L5

Holmberg E., 1941, ApJ, 94, 385

Jenkins A., Frenk C. S., White S. D. M., Colberg J. M., Cole S., Evrard A. E., Couchman H. M. P., Yoshida N., 2001, Monthly Notices of the Royal Astronomical Society, 321, 372–384

Joshi G. D., Pontzen A., Agertz O., Rey M. P., Read J., Renaud F., 2024, VINTERGATAN-GM: How do mergers affect the satellite populations of MW-like galaxies? (`arXiv:2307.02206`), `https://arxiv.org/abs/2307.02206`

Klypin A. A., Trujillo-Gomez S., Primack J., 2011, The Astrophysical Journal, 740, 102

Knebe A., et al., 2011, Monthly Notices of the Royal Astronomical Society, 415, 2293–2318

Mo H., van den Bosch F., White S., 2010a, Gravitational Collapse and Collisionless Dynamics. Cambridge University Press, pp 215–261

Mo H., van den Bosch F., White S., 2010b, Formation and Structure of Dark Matter Halos. Cambridge University Press, p. 319–365

Moore B., 2001, in AIP Conference Proceedings. AIP, p. 73–82, doi:10.1063/1.1419537, `http://dx.doi.org/10.1063/1.1419537`

More S., Kravtsov A. V., Dalal N., Gottlöber S., 2011, The Astrophysical Journal Supplement Series, 195, 4

Peebles P. J. E., 1969, ApJ, 155, 393

Peebles P. J. E., 1971, A&A, 11, 377

Peirani S., et al., 2017, Monthly Notices of the Royal Astronomical Society, 472, 2153–2169

Planck Collaboration ESA 2013b, Cosmic Microwave Background Map from the Planck Mission, `https://planck.ipac.caltech.edu/image/planck13-001a`

Planck Collaboration ESA 2013a, Refining the Ingredients of Our Universe (Planck13-001e), `https://planck.ipac.caltech.edu/image/planck13-001e`

Porciani C., Dekel A., Hoffman Y., 2002a, Monthly Notices of the Royal Astronomical Society, 332, 325

Porciani C., Dekel A., Hoffman Y., 2002b, Monthly Notices of the Royal Astronomical Society, 332, 339

Stewart K. R., Brooks A. M., Bullock J. S., Maller A. H., Diemand J., Wadsley J., Moustakas L. A., 2013, The Astrophysical Journal, 769, 74

Stopyra S., Pontzen A., Peiris H., Roth N., Rey M. P., 2021, The Astrophysical Journal Supplement Series, 252, 28

Teyssier R., 2002, A&A, 385, 337

Toomre A., Toomre J., 1972, ApJ, 178, 623

Turk M. J., Smith B. D., Oishi J. S., Skory S., Skillman S. W., Abel T., Norman M. L., 2011, The Astrophysical Journal Supplement Series, 192, 9

Vitvitska M., Klypin A. A., Kravtsov A. V., Wechsler R. H., Primack J. R., Bullock J. S., 2002, The Astrophysical Journal, 581, 799–809

Weinberg D. H., Colombi S., Davé R., Katz N., 2008, The Astrophysical Journal, 678, 6–21

White S. D. M., 1984, ApJ, 286, 38

White M., 2001, Astronomy & Astrophysics, 367, 27–32

White S. D. M., Rees M. J., 1978, MNRAS, 183, 341

Yang H., Gao L., Frenk C. S., Grand R. J. J., Guo Q., Liao S., Shao S., 2023, MNRAS, 518, 5253

Zel'dovich Y. B., 1970, A&A, 5, 84

Zolotov A., et al., 2012, ApJ, 761, 71

von Hoerner S., 1960, Z. Astrophys., 50, 184